A multi-fidelity modelling approach for evaluation and optimization of wing stroke aerodynamics in flapping flight

Lingxiao Zheng[1], **Tyson L. Hedrick**[2] **and Rajat Mittal**[1,†]

[1]Department of Mechanical Engineering, the Johns Hopkins University, Baltimore, MD 21218, USA

[2]Department of Biology, University of North Carolina at Chapel Hill, Chapel Hill, NC 27599, USA

The aerodynamics of hovering flight in a hawkmoth (*Manduca sexta*) are examined using a computational modelling approach which combines a low-fidelity blade-element model with a high-fidelity Navier–Stokes-based flow solver. The focus of the study is on understanding the optimality of the hawkmoth-inpired wingstrokes with respect to lift generation and power consumption. The approach employs a tight coupling between the computational models and experiments; the Navier–Stokes model is validated against experiments, and the blade-element model is calibrated with the data from the Navier–Stokes modelling. In the first part of the study, blade-element and Navier–Stokes modelling are used concurrently to assess the predictive capabilities of the blade-element model. Comparisons between the two modelling approaches also shed insights into specific flow features and mechanisms that are lacking in the lower-fidelity model. Subsequently, we use blade-element modelling to explore a large kinematic parameter space of the flapping wing, and Navier–Stokes modelling is used to assess the performance of the wing-stroke identified as optimal by the blade-element parameter survey. This multi-fidelity optimization study indicates that even within a parameter space constrained by the animal's natural flapping amplitude and frequency, it is relatively easy to synthesize a wing stroke that exceeds the aerodynamic performance of the hawkmoth wing stroke. Within the prescribed constraints, the optimal wing stroke closely approximates the condition of normal hover, and the implications of these findings on hawkmoth flight capabilities as well as on the issue of biomimetic versus bioinspired design of flapping wing micro-aerial vehicles, are discussed.

Key words: biological fluid dynamics, computational methods, swimming/flying

1. Introduction

The development of flapping wing micro-aerial vehicles (MAVs) in recent years has been inspired primarily by flying insects and birds (see Ellington *et al.* 1996; Lehmann & Dickinson 1997; Dickinson, Lehmann & Sane 1999; Fry, Sayaman & Dickinson 2003; Warrick, Tobalske & Powers 2005; Wood 2008; Floreano *et al.* 2009). Design of such MAVs can either follow a 'biomimetic' approach where the designer

† Email address for correspondence: mittal@jhu.edu

mimics as closely as possible all features of the corresponding biological system or it can follow a 'bioinspired' approach where key features of the biological system are identified, their function understood and the feature then modified and/or simplified for adoption into the engineered system. The latter approach is based on the recognition that an engineered system usually has design objectives that differ from those of the biological flyer. Biological organisms are a result of evolution through natural selection which does not necessarily produce designs that are 'optimal' in terms of performance metrics relevant to a MAV designer. The ultimate objective of any biological organism is to successfully reproduce and pass along its genetic information to subsequent generations; this may be accomplished in a multitude of ways, some detrimental to improved flight performance. For example, once adequate flight performance is achieved, animals may evolve to direct resources toward reproduction rather than further improvements in flight ability. In contrast, an engineered MAV might have more specific design objectives in terms of range, payload, etc. In addition, evolution by natural selection is a dynamic process which is constantly affected by an ever-changing environment, and biological designs often include vestigial or redundant features that increase complexity without enhancing performance. This implies the possibility of learning from biological flyers and then subsequently simplifying their design and/or improving on their performance.

The bioinspired design approach also recognizes that engineered and biological flyers differ with respect to the limitations and capabilities of the materials, actuators, control systems, power and sensory modalities that are available to them, and that simply mimicking nature might not work. An often-cited example in this regard is the singular lack of rotary motors in biological organisms (with the notable exception of the molecular-scale rotary motor powering bacterial flagella (Berg 2003)) and the preponderance of such motors in engineered systems. Thus, a flapping wing in a biological flyer that is designed to be powered by muscles (i.e. linear motors) might have to be modified to work in conjunction with a rotary mechanism.

The bioinspired design approach requires tools that can evaluate candidate designs and search for optimal (or at least higher-performing) solutions. Evaluation and optimization through experiments is a possibility, but can be prohibitively expensive given the dimensionality and size of the parameter space that often needs to be explored. Computational modelling seems to be well suited for this purpose, but here too, one has to compromise between model fidelity and computational effort. In the context of the aerodynamic design of flapping wings, the topic of the current paper, modelling tools range from low-fidelity, low-cost blade-element models (BEM) to high-fidelity, high-effort Navier–Stokes (NS) solutions.

BEMs, occasionally also known as strips models, operate by dividing the wing into a set of chordwise strips and computing the fluid dynamic forces produced by those elements from their instantaneous velocity about the animal or vehicle, the velocity of the surrounding fluid and the angle of incidence between the wing element and fluid (Osborne 1951). These values, which may be generated as part of a simulation or from kinematic analysis of an organism, are then put into a function relating the angle of incidence to wing performance, i.e. coefficients of lift and drag. The forces thus generated are then summed across all wing elements, and the basic BEM also modified to account for other instantaneous forces such as those due to fluid added mass or wing rotation (Berman & Wang 2007). As such, BEM are a form of quasi-steady analysis, where the aerodynamic performance of the wing is assumed to be independent of all events both before and after the instant under consideration. Thus, simple BEMs cannot accurately model time-history-related

phenomena such as wing–wing (Weis-Fogh 1973) or wing–wake (Dickinson *et al.* 1999) interactions in flying insects, and post-stall dynamics of typical aerofoils (Delaurier 1993). BEMs also lack any notion of the vortex dynamics underlying force production by flapping foils and are thus unaffected by suboptimal vortex shedding frequencies (Triantafyllou, Triantafyllou & Grosenbaugh 1993). Furthermore, BEM depend critically on the function relating element angle of incidence to aerodynamic forces, typically determined by a separate computational or mechanical modelling study, although some researchers apply the BEM approach in reverse, calculating the minimum average coefficient-of-lift required to support an animal given observations of its flapping movement (Osborne 1951; Pennycuick, Hedenstrom & Rosén 2000).

Despite these weaknesses, BEMs have seen wide application to both biological and engineered systems, largely because of their computational simplicity and amenability of combining experimental recordings with the modelling approach. Computational simplicity allowed early application before the wide use of digital computers (e.g. Osborne 1951; Blake 1979) and in more recent times, has facilitated large-scale parameter optimization studies in animal swimming (Walker & Westneat 2000) and flying (Hedrick & Daniel 2006; Berman & Wang 2007) as well as wind turbines (Benini & Toffolo 2002).

An example of bioinspired design based on NS modelling can be found in the work of Bozkurttas *et al.* (2009) and Tangorra *et al.* (2010). In these studies, NS modelling was coupled with a proper orthogonal decomposition (POD)-based analysis of the fin kinematics to significantly reduce the design complexity of a bioinspired robotic pectoral fin, while preserving key features of its hydrodynamic performance. However, NS modelling, especially for realistic three-dimensional cases, is computationally expensive and cannot be used for an exhaustive parameter sweep.

Given the complementary nature of these modelling techniques, a seemingly viable approach to bioinspired design is one that combines the two techniques; in this approach, NS modelling would be used to calibrate the BEM for a particular flapping-wing configuration; BEM would then be used for an exhaustive survey of the parameter space and to identify solutions that are optimal; finally, NS modelling would provide a more accurate assessment of the solution(s) identified as optimal by the BEM. To the best of the authors' knowledge, such a multi-fidelity study for the evaluation and optimization of flapping wings has not been conducted previously and one objective of the current paper is to explore the viability of such an approach for the particular case of flight with flapping wings. We choose hovering flight in a hawkmoth (*Manduca sexta*) as the source of our bioinspired approach; we show that the wing stroke employed by this insect for hovering is suboptimal in terms of aerodynamic performance and we use the multi-fidelity approach to search for optimal solutions.

2. Approach

The approach employed in the current study is described here. This includes a discussion of the animal model used, details of the experimental set-up and flight measurements, a description of the BEM and NS modelling approaches used in the current study, as well as the techniques used for optimization.

2.1. *Animal model*

The hawkmoth species examined here, *Manduca sexta*, is a relatively large ($\sim$2 g body mass, 10 cm wing span), nectivorous insect with a number of characteristics

that make it and its close relatives particularly useful subjects in laboratory studies of animal flight. Specifically, the moths: (i) are readily available year-round from domestic colonies; (ii) exhibit controlled hovering flight behaviour when feeding from a nectar source, permitting easy experimental application of techniques ranging from kinematic analysis to digital particle image velocimetry (PIV); (iii) are able to carry a substantial payload of experimental apparatus to provide an on-board measurement capability (Wang, Ando & Kanzaki 2008); and (iv) are well-characterized organisms, with ongoing research in areas ranging from hormonal and neural control to ecology. Aerodynamically, hawkmoths exhibit many common features of insect flight, including a strong leading-edge vortex (LEV), first discovered in this species (Ellington *et al.* 1996), and substantial inertial and aeroelastic deformation of the wing surface (Combes & Daniel 2003). For these reasons, the aerodynamics of hawkmoth flight have been studied by many groups applying a variety of techniques including kinematics, smoke visualization, dynamically scaled mechanical models, computational fluid dynamics (CFD) and two-dimensional PIV (Willmott & Ellington 1997*a*; Willmott, Ellington & Thomas 1997; Liu *et al.* 1998; Bomphrey *et al.* 2005).

The hawkmoth recorded and modelled in this study was a male from the colony at The University of North Carolina at Chapel Hill, recorded on the third day post-eclosure. The moth was conditioned to hover and fed from an artificial flower containing a sugar solution (4:1 water:sugar) placed more than 10 chord lengths above the floor of the flight chamber. Recordings were collected once the moth was sufficiently trained to regularly approach the flower. This individual moth weighed 1.39 g at the time of recording, had a 9.86 cm wingspan, 17.5 cm^2 total wing area and a non-dimensional second moment of wing area of 0.51 for the combined fore and hind wings spread as in mid-downstroke. The moth was not sacrificed after recording, so specific body-segment masses were not available and were assumed to follow the distribution established for this colony. *A prior* examination of the segment mass proportions from the animals in the UNC colony revealed the following mass distribution: abdomen $50.1 \pm 5.4\%$ of total mass (mean $\pm$ standard deviation, $n = 10$), thorax and head $45.1 \pm 3.6\%$, wings $4.8 \pm 0.9\%$. The centre-of-mass (CoM) for each of these segments was determined for a male moth from the UNC colony by separating them and suspending them from a string at several points on the periphery. The CoMs of the abdomen and head plus thorax segments were near the geometric centre of the segments while the wing CoM was closer to the root than to the geometric centre.

2.2. *Experimental set-up and kinematic analysis*

The moth was recorded while hovering in front of the artificial flower (but not in contact with it) in a 0.37 m^3 glass-walled flight chamber (figure 1*a*) by a set of three orthogonally positioned high-speed video cameras (2× Phantom v7.1 and 1 Phantom v5.1, Vision Research, Wayne, NJ) operating at 1000 frames per second and a shutter duration of 300 μs. The flight chamber was strongly lit at the infrared wavelength of 760 nm to permit operation of the cameras at these shutter speeds, but was only dimly lit in the visible spectrum (85 lux) to accommodate the behaviour of *Manduca sexta*, which are typically active at twilight. Figure 1(*b*) shows sample frames that were taken from the high-speed cameras. The cameras were calibrated for three-dimensional reconstruction using the direct linear transformation (DLT) method (Hedrick 2008).

Three-dimensional kinematics were obtained by tracking the location of the left and right wing base, wing tip and the forewing notch on the trailing edge of the wing, the centre of the head, the thorax–abdomen junction and the tip of the abdomen
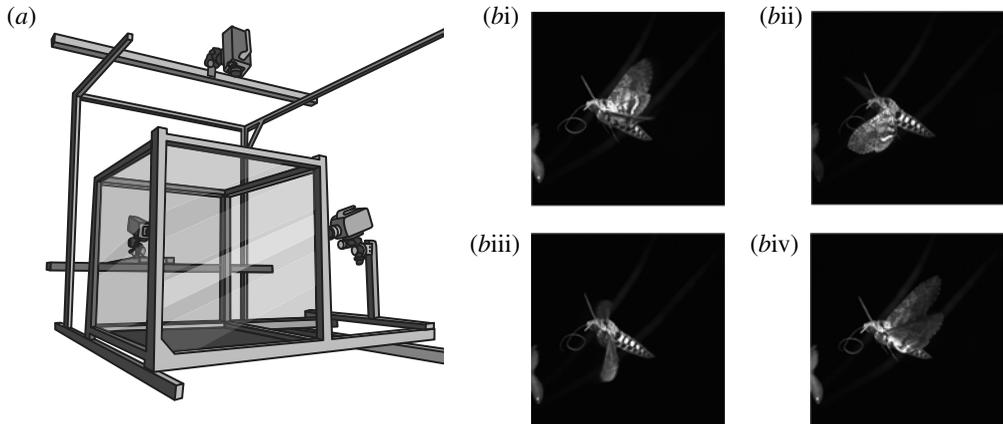
FIGURE 1. The flight enclosure and apparatus used to record the moth and sample images from the high-speed cameras. (*a*) The moth flew in the centre of a 0.37 m^3 glass-walled flight chamber in the view of three synchronized high-speed (1000 Hz) video cameras. Lighting for the high-speed cameras was provided by eight infrared light-emitting diodes positioned inside the chamber. (*b*) Sample images from the video recordings captured in the apparatus showing a moth in four stages of a wingbeat cycle: (i) early downstroke; (ii) late downstroke; (iii) middle upstroke; and (iv) late upstroke.

through 4.5 successive hovering wingbeats including the wingbeat used for the NS analysis. Kinematics are inherently noisy data due to discretization at the sensor level and introduction of operator error as points are recognized and marked in the image, whether the marking is performed by human or computer. Thus, the body segment landmarks were marked independently by four different researchers and the differences among outputs from different researchers used to quantify the measurement error rate. This error rate was used along with a quintic smoothing spline to low-pass filter the position measurement time series to the smoothest (i.e. smallest magnitude second-derivative) curve consistent with the measurement and error rate. Next, the smoothed points (and segment mass information described above) were used to compute the three-dimensional location of the CoM for each of the four body segments (left wing, right wing, thorax (including head) and abdomen). We then computed the segment accelerations by taking the second derivative with respect to time and adding a gravitational acceleration of 9.81 m s^{-2}. These three-dimensional accelerations were then converted to forces by multiplying by the segment masses and added together to reveal the net instantaneous aerodynamic force exerted on the moth, in essence quantifying the instantaneous acceleration of the CoM of the whole animal. Finally, to quantify the variation among flaps, we divided the digitized sequence into four complete phase-matched flapping cycles, and computed the phase-specific standard deviation among flaps for the total force measurements (figure 2). This variation among strokes was used as a proxy for the uncertainty in the measurement of any individual stroke. Camera calibration and kinematics analysis were performed using the DLTdv package (Hedrick 2008) for MATLAB (The Mathworks, Natick, MA).

2.3. *Matching wing kinematics*

Using the images from the calibrated high-speed video apparatus (figure 1*b*), we reconstructed the flexible wings and body as a mesh suitable for input into our
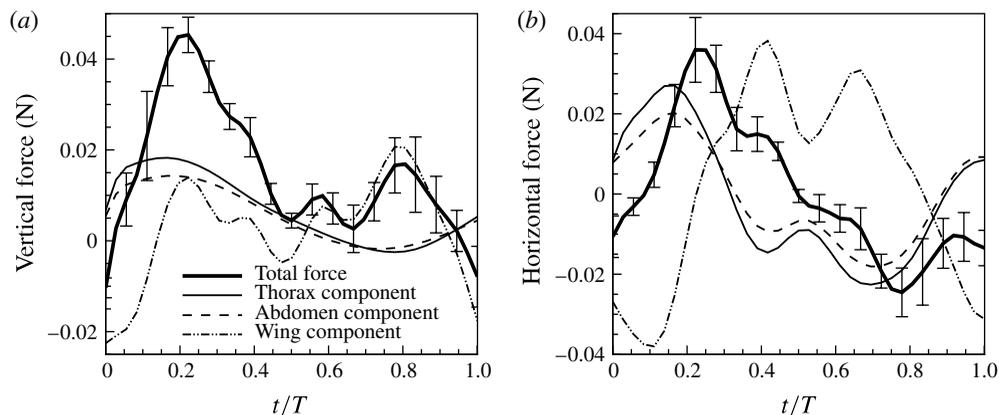
FIGURE 2. Instantaneous vertical (*a*) and horizontal (*b*) forces measured from the kinematic reconstruction of the flapping moth. The heavy black line shows the net aerodynamic force, the error bar around it shows ± one standard deviation measured from the variation among the four wingbeats in the flapping sequence. The other lines show the forces recovered from the acceleration of the individual body segments. The wings typically move in the opposite direction of the head and thorax, such that the magnitude and even direction of the net forces acting on the moth cannot be determined from the movements of a single location on the animal. The downstroke portion of the flapping cycle is from t/T of 0 to 0.55; upstroke is from 0.56 to 1.0.

CFD solver. First, Gridgen (Pointwise, Inc., Fort Worth, TX) was used to reconstruct the hawkmoth wing mesh with zero thickness. Because the fore and hind wings do not significantly change their positions relative to each other during the flapping cycle, they were modelled as a single surface. Next, the three-dimensional modelling, animation, visual effects and rendering software Maya (Autodesk Inc., San Rafael, CA) was used to create an 'animation' of the moth in flight where the wing kinematics were matched very closely to 16 different instances in the flapping cycle as observed in the high-speed videos in three views. Figure 3 shows the match between the images and our model at one instant in time. Deformation was added to the wing in Maya by positioning a set of internal wing spars analogous to the veins of the actual moth. This animation was then interpolated in time with a cubic spline to produce a high-frame-rate input into the CFD solver. The geometry of the moth body was constructed from a high-resolution (0.005 in. precision) NextEngine (NextEngine, Inc., Santa Monica, CA) laser scanner.

2.4. *Navier–Stokes flow modelling*

A sharp-interface immersed-boundary method (Mittal & Iaccarino 2005) described by Mittal *et al.* (2008) and Seo & Mittal (2011) has been used in these simulations. The governing equations are the three-dimensional unsteady, viscous incompressible NS equations:

$$\frac{\partial u_i}{\partial x_i} = 0; \quad \frac{\partial u_i}{\partial t} + \frac{\partial u_i u_j}{\partial x_j} = -\frac{1}{\rho}\frac{\partial p}{\partial x_i} + \nu\frac{\partial}{\partial x_j}\left(\frac{\partial u_i}{\partial x_j}\right) \tag{2.1}$$

where u_i are the velocity components, p is the pressure and ρ and ν are the fluid density and viscosity, respectively. The above equations are discretized using a cell-centred, collocated (non-staggered) arrangement of the primitive variables (u_i, p). In
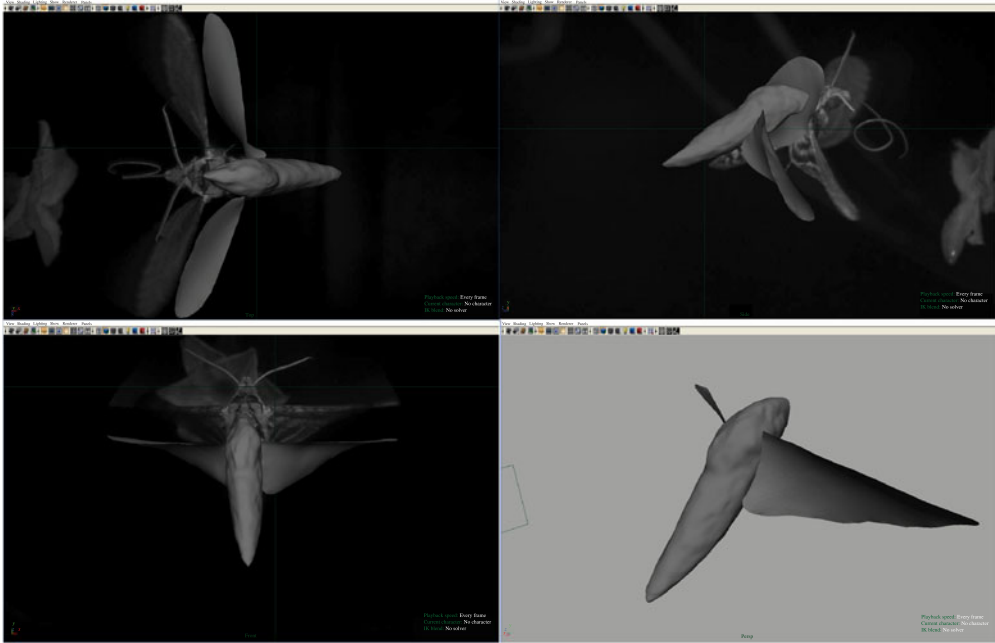
FIGURE 3. (Colour online) Comparison of the reconstructed moth model with three video views of the actual moth at the beginning of the upstroke.

addition to the cell-centre velocities (u_i) that satisfy the momentum equations, the face-centre velocities, which satisfy mass conservation, are also computed (Ye *et al.* 1999). A fractional-step method (Van Kan 1986; Zang, Street & Koseff 1994) is used for the time-advancement of the above equation.

The effect of the immersed boundary on the flow is incorporated by using a multi-dimensional ghost-cell methodology. This method falls in the category of sharp-interface discrete forcing immersed boundary methods (Mittal & Iaccarino 2005). The current method employs an unstructured grid with triangular elements to represent the surface of three-dimensional bodies such as the insect wings which is immersed into the Cartesian volume grid. The ghost cells are defined as the cells inside the solid that have at least one neighbour in the fluid. The second-order accurate discretization on the body surface along with the second-order accuracy of the fluid cells leads to second-order local and global spatial accuracy in the computations (Mittal *et al.* 2008). The accuracy of the solver for zero-thickness bodies, such as insect wings, has been demonstrated by simulating flow past a suddenly accelerated plate and comparing results with available experiments and simulations (Mittal *et al.* 2008). More details regarding such immersed-boundary methods can be found in the work of Ye *et al.* (1999), Udaykumar *et al.* (2001) and Mittal & Iaccarino (2005).

2.5. *Blade-element model*

BEMs of flapping flight operate under the assumption that the total instantaneous force on a wing can be computed as the sum of forces acting on a set of infinitesimal chordwise strips. The forces themselves are provided by reference to quasi-steady aerodynamic models of varying complexity, but typically require wing orientation, a flow velocity vector, a wing shape and a set of force coefficients as inputs.

Early models used quasi-steady force coefficients derived from measurements made on animal wings fixed in static flows (Osborne 1951; Willmott & Ellington 1997*b*). With further improvement in understanding of the aerodynamic properties of flapping wings, BEMs began to take advantage of quasi-steady aerodynamic force models derived from dynamically scaled flapping robots (Dickinson *et al.* 1999; Usherwood & Ellington 2002). When running with flapping kinematics similar to those used by actual flying animals, BEMs based on these experimentally derived quasi-steady models provide sufficient force to support body weight (Hedrick & Daniel 2006; Berman & Wang 2007). Comparing with CFD models, the chief advantage of all BEMs is their simplicity, which allows rapid computation and facilitates studies that require a large number of evaluations of some flight characteristic, e.g. flight control (Hedrick & Daniel 2006) or energy minimization (Berman & Wang 2007).

In this paper, a previously established BEM of hawkmoth flapping flight (Hedrick & Daniel 2006) which incorporates quasi-steady approximations of the aerodynamic forces due to wing translation (Dickinson *et al.* 1999), rotation of the wing about its spanwise axis (Sane & Dickinson 2002) and added mass was employed. In this model, the force on any given strip is calculated based on its angle of incidence with respect to the local flow, and its angular velocity and acceleration.

For the purpose of optimizing the wing stroke, we assume that the wing of the hawkmoth in hovering flight can be approximated as a rigid flat plate. While previous as well as the current (see figure 3) studies clearly show noticeable spanwise and chordwise curvature as well as spanwise twist during the stroke (Zeng, Hao & Kawachi 2000; Sunada *et al.* 2002; Wang *et al.* 2003; Walker, Thomas & Taylor 2008), a flat-plate approximation has often been used for these insects (Willmott & Ellington 1997*a*; Liu & Aono 2009). For a rigid, flat-plate wing, the wing position is specified in the spherical (ϕ, θ) coordinate of the wing tip with respect to the wing root and a spanwise rotation α about the axis extending from the wing root to the wing tip specifying the wing pitch. For a given motion of the wing, the total force is calculated as the sum of the blade-element estimates of force due to wing translation, force due to wing rotation about the spanwise axis and the added-mass acceleration reaction. As given by Hedrick & Daniel (2006), the force due to wing translation is computed as

$$F_{trans} = 0.5 \rho R \bar{c} \int_0^1 C_{trans}(\hat{r}) U^2(\hat{r}) \hat{c}(\hat{r}) \, \mathrm{d}(\hat{r}) \qquad (2.2)$$

where ρ is air density (1 kg m^{-3}), R (shown in figure 4*c*) is the wing length, U is the instantaneous velocity of the flow across the wing, C_{trans} is the aerodynamic force coefficient, $\hat{r}$ is the non-dimensional radial position along the wing, $\bar{c}$ is the average chord-length and $\hat{c}$ is the non-dimensional chord length (scaled to $\bar{c}$), and the aerodynamic force F_{trans} is assumed to act perpendicular to the wing surface.

Following Sane & Dickinson (2002), the force due to wing rotation about the span axis is estimated as

$$F_{rot} = C_{rot} \rho U_T \dot{\alpha} \bar{c}^2 R \int_0^1 \hat{r} \hat{c}^2(\hat{r}) \, \mathrm{d}(\hat{r}) \qquad (2.3)$$

where C_{rot} is the force coefficient for wing rotation, U_T is the instantaneous velocity of the wing tip, $\dot{\alpha}$ is the wing's instantaneous span-axis rotational velocity, $\bar{c}$ is mean chord length and $\hat{c}$ is the non-dimensional chord length for a particular strip. The
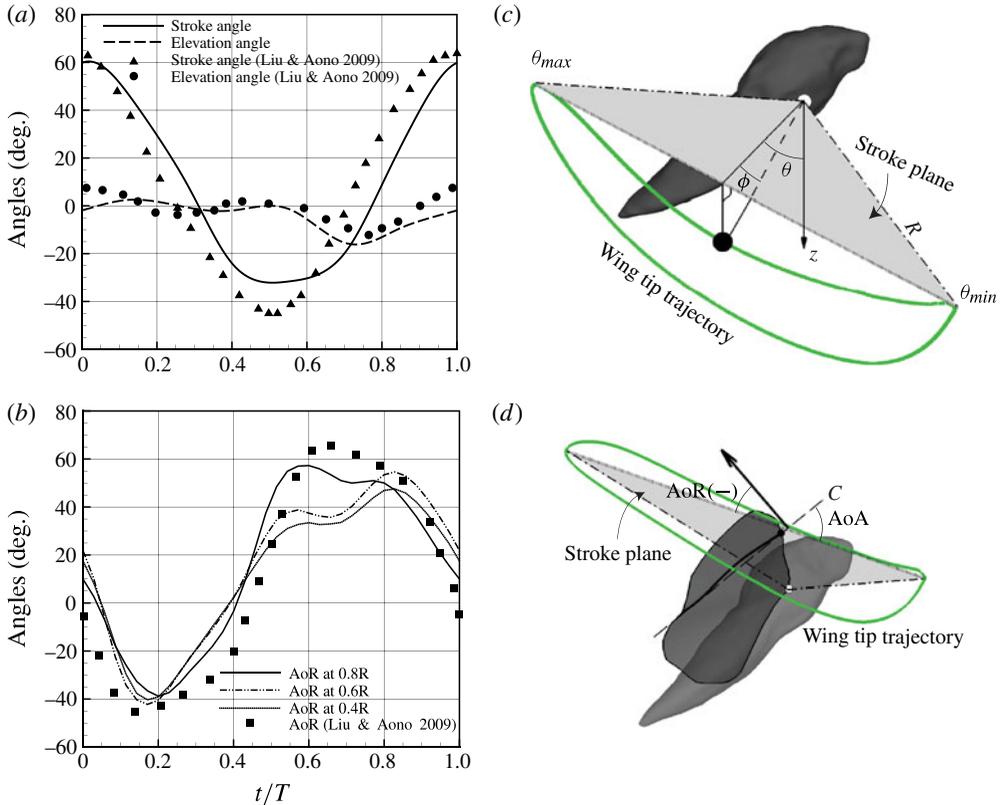
FIGURE 4. (Colour online) Wing kinematics for the hawkmoth in hover: (*a*) schematic showing stroke and elevation angles for the current study as well as that of Liu & Aono (2009); (*b*) comparison of AoR relative to stroke plane between current work and Liu & Aono (2009). The AoR along the spanwise direction is not constant in this work due to the wing twist; (*c*) definition of stroke angle (θ) and elevation angle (ϕ). Wing length R is defined as the distance between wing root and wing tip; (*d*) definition of AoR and AoA. Cr is the wing curvature obtained by the plane which is vertical to the line joining wing root and tip. C is the line joining the leading and trailing edge of Cr and the black dot represents the leading-edge. AoR is defined as the angle between stroke plane and the line perpendicular to the wing surface (shown as the line with an arrow). During downstroke, AoA equals to AoR(−) plus 90°; during upstroke, AoA equals to 90° minus AoR(+).

forces due to added-mass were estimated based on the following formula:

$$F_{acc} = \frac{\rho\pi\bar{c}^2R^2}{4} \int_0^1 \hat{r}\hat{c}^2(\hat{r})\,\mathrm{d}(\hat{r})[\ddot{\Phi}\sin\alpha + \dot{\Phi}\dot{\alpha}\cos\alpha] + \frac{\rho\pi R\bar{c}^3\ddot{\alpha}}{16}\int_0^1 \bar{c}^3(\hat{r})\,\mathrm{d}(\hat{r}) \quad (2.4)$$

where $\dot{\Phi}$ and $\ddot{\Phi}$ are the wing's overall instantaneous angular velocity and acceleration, α is the wing's span-axis angular position, $\dot{\alpha}$ is the wing's span-axis rotational velocity and $\ddot{\alpha}$ is the wing's span-axis rotational acceleration. Given that the pressure force dominates viscous force for the situations of interest here, we assume that the net force estimated above acts normal to the wing surface and we decompose this net force into a vertical (lift) and lateral (drag) component.

2.6. *Optimization techniques*

As will be discussed in § 4.1, we use harmonic wing motions represented by eight independent parameters within a combined genetic algorithm (GA) (Krishnakumar 1989) and simplex search (Nelder & Mead 1965) framework to synthesize wing strokes which might outperform the stroke from the actual moth according to different criteria. These cost function criteria also include constraints to prevent the optimization routines from adopting wing strokes with greater overall flapping amplitude or higher flapping frequency than used by a real animal, thereby keeping the optimization within some of the constraints which the actual animal appears to operate under. While larger frequencies or amplitudes are easily shown to lead to greater aerodynamic force or efficiency in BEMs, they also increase the inertial power requirements of flapping which were not modelled here.

In brief, the GA creates a population of unique individuals with different, randomly selected genotypes of flapping kinematic parameters. The performance of these individuals is then evaluated using the cost function of our choosing and high-fitness individuals propagated into the next generation as: (A) clones; (B) clones with mutations or changes to a few parameters; and (C) by mixing their parameters with those of other high fitness individuals. The next generation is filled randomly with these novel individuals and the process repeated until it converges to a local minimum of the cost function, with the random nature of the GA allowing it to reject poor local minima. After the GA converges, the individual with the highest fitness are used as the basis for a gradient-based search to find the local minima. These individuals are selectively transferred to the NS modelling to more accurately assess their performance.

3. Validation of Navier–Stokes modelling

The underlying assumption in this multi-fidelity approach is that the NS approach provides an accurate solution of the aerodynamics of flapping flight in the regime relevant to a hovering hawkmoth. In order to confirm this, the NS approach has to be validated carefully and resolution requirements established. In this section, we describe this validation process and the results from the validation. Many prior studies applying CFD to animal flight (e.g. Aono, Shyy & Liu 2009; Liu & Aono 2009) took the approach of comparing the whole-stroke mean lift to the weight of the animal. While this type of validation is a good starting point, it is not sufficient to demonstrate that the animal and simulation produce similar temporal variation in forces. Correct prediction of these temporal variations is crucial both for connecting force production with specific aerodynamic features as well as for accurate estimation of aerodynamic power.

3.1. *Experimental estimation of aerodynamic forces*

The net instantaneous aerodynamic force acting on the moth was obtained from the calibrated video sequences as described above along with the accelerations of the different body segments of the moth. As shown in figure 2, the moth produces substantially greater net vertical force during the downstroke phase of the flapping cycle ($t/T < 0.55$) compared with the upstroke phase. Vertical force peaks at a t/T of approximately 0.25, or shortly before mid-downstroke. A second vertical force peak occurs near mid-upstroke (phase $\sim$0.8), but the magnitude of this force is less than half of that during downstroke. Minimal or even slightly negative net vertical forces are generated at the wing turnaround events near the ends of downstroke and upstroke. With respect to horizontal force, the magnitude of force generated in the two halves of

the stroke cycle is similar, although opposite in sign and also tends to peak near the midpoint of each half stroke. The horizontal force generated in downstroke is directed rearward, pushing the moth backward, while horizontal force in upstroke is directed forward.

The experimental results shown are phase-averaged over four consecutive flapping cycles that were recorded in the experiment where the moth was hovering in place with no significant lateral or vertical motion. These are also the same cycles that were used to generate the flapping-wing model for the flow simulations. The cycle-to-cycle variation in these flaps were used to estimate the variation (shown as bars in figures 2 and 8) in the experimental values and these are indicative of the level of variability and uncertainty that is inherent in these biological experiments. Some of this variability is likely associated with measurement error but some comes from the fact that there are indeed noticeable cycle-to-cycle variations in the wingbeat even in a case where the insect seems to be hovering in place.

3.2. *Wing kinematics during flapping flight*

For the particular moth examined in this work, the body weight, wing length, mean chord length, flapping frequency, wingbeat amplitude and the stroke plane angle are $m = 1.39$ g, $R = 4.93$ cm, $\bar{c} = S/2R = 1.77$ cm, $f = 1/T = 25$ Hz, $\theta_A = 100.3°$ and $\beta = 21.8°$, respectively. The average tip velocity during one cycle is $U = 2\theta_A fR = 4.3$ m s^{-1}. Based on these, the wing-flapping Reynolds number was estimated to be $Re = U \times \bar{c}/\nu = 5297$. The above parameters are all within the range of previous records for hovering hawkmoths (Willmott & Ellington 1997*a*).

The comparison of wing kinematics between the current study and previous model with flat-plate wings (Liu & Aono 2009) is presented in figure 4(*a,b*). The definition of different angles is shown in figure 4(*c,d*). Figure 4(*a*) indicates that the elevation and stroke angles match reasonably well between the two models except that the current model shows a smaller and wider peak of the stroke angle at t/T from 0.4 to 0.6. Since the angle of rotation (AoR), defined as α in this work, is not constant due to the wing twist in the current study, the AoRs at three spanwise location (0.4R, 0.6R and 0.8R) is presented in figure 4(*b*) and compared with that from the model of Liu & Aono (2009). A difference in AoR of $\sim20°$ along the spanwise direction is observed at $t/T \sim 0.6$. Similar wing twist, which is quantified by AoR, was also reported by Willmott & Ellington (1997*a*). Furthermore, from the relationship between AoR and angle of attack (AoA), we estimate that for the current study, the AoA is $\sim60°$ during the middle of downstroke ($t/T \sim 0.25$) and 30° during mid-upstroke ($t/T \sim 0.8$). Also, it is noted that during downstroke, the AoA of the current model is approximately 10° larger than the model of Liu & Aono (2009). Figure 4(*d*) also indicates that the wings flap with positive camber, which was also observed previously (Sunada *et al.* 2002; Young *et al.* 2009; Nakata & Liu 2012; Zheng, Mittal & Hedrick 2013). The ratio of maximum camber at 0.8R to the corresponding chord length is approximately 5 % during mid-downstroke and 15 % during mid-downstroke for the current hawkmoth wing model.

3.3. *Computational setup*

Figure 5(*a*) shows the constructed realistic wing–body model immersed in the three-dimensional non-uniform Cartesian grid. The coordinate directions, which are also shown in figure 5(*b*), are as follows: X is in the horizontal direction with $+X$ pointing towards the rear of the moth; Z is the spanwise direction with $+Z$ pointing to the moth's left wing (viewed from behind the moth); and Y is the vertical direction
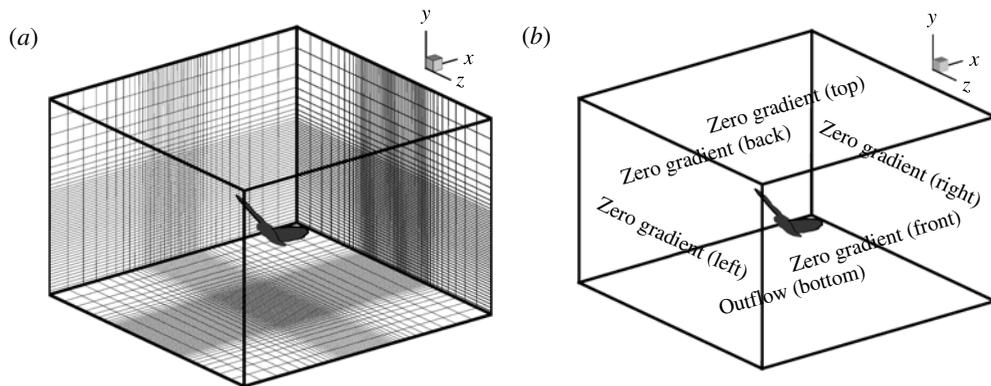
FIGURE 5. The constructed realistic wing-body model immersed in the three-dimensional non-uniform Cartesian grid (*a*) and boundary conditions for the simulation (*b*).

with $+Y$ pointing upward. The wings in the validation study are modelled as deforming membranes and the body (comprising the head, abdomen and thorax) is treated as a non-deforming and stationary object.

Figure 5(*b*) shows the boundary conditions applied on the computational domain boundaries. On all of the boundaries except the bottom boundary, a far-field boundary condition which amounts to specifying the streamwise (vertical) velocity component to zero and setting the normal gradients of the other velocity components to zero is applied. The flapping wings of the moth generate a pair of vortex-ring-like structures below the body, which will be shown later. Thus, on the bottom boundary, a convective boundary condition which allows the vortex structures to exit the domain without any spurious reflections was applied (Mittal & Iaccarino 2005). The final domain size normalized by the mean chord length $\bar{c}$ is $25 \times 20 \times 25$ and this large domain ensures that the boundaries do not have any significant effect on the computed results. As shown in figure 5(*a*), the grid is designed to provide high resolution in the region around body as well as the wake which is expected to develop below the body and wings. This grid was developed in an iterative fashion starting from a sequence of coarser grids. Computed results on these earlier meshes were examined and the resolution in selected regions increased until the key features such as forces and vortex structures became essentially independent of the grid. The final (baseline) grid adopted here has $128 \times 128 \times 128$ points. The grid size $\Delta x = \Delta y = \Delta z = 0.1$ mm corresponds to 45 grids across the span and 20 across the chord-wise direction on the wing surface.

Three additional simulations on different grids were carried out to assess the convergence of the computed flow. Simulation 1 was carried out on a grid which had 70 % more grid points than the baseline grid and simulation 2 was carried out on a mesh with 50 % less grid points than the baseline grid. Both of these simulations produced a maximum 1 % difference from the baseline in mean lift and root-mean-square (r.m.s.) values of lift and drag. Finally, simulation 3 was carried out on a grid where the number of grid points in each direction around the wing were twice those in simulation 2. This simulation also produces mean lift and r.m.s. lift and drag that are within 1 % of simulation 2 and taken together with the other simulations, provide clear proof of the grid convergence of the current results.

The time step chosen for the current simulations is $\sim 5.7 \times 10^{-5}$ s which corresponds to a Courant-Friedrichs-Lewy (CFL) number of ~ 0.48. With this time step, each
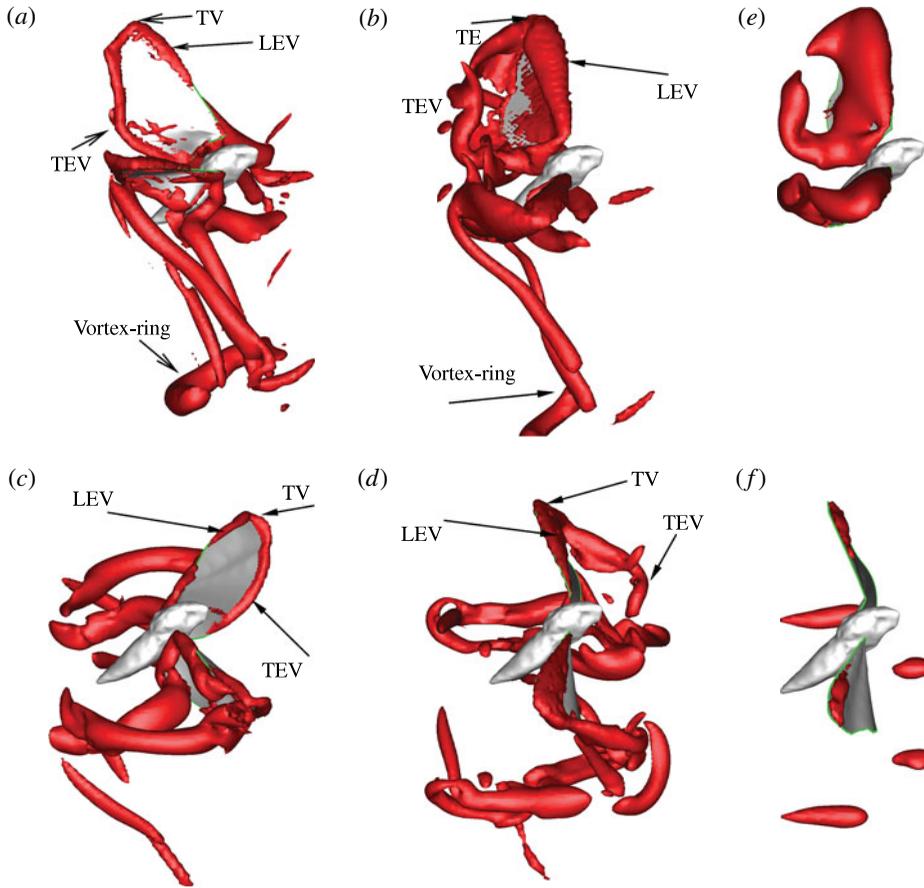
FIGURE 6. (Colour online) Vortex structures generated by the hovering moth at: (*a*) $t/T = 0.1$; (*b*) $t/T = 0.25$; (*c*) $t/T = 0.53$; and (*d*) $t/T = 0.82$. All of the three-dimensional vortex topology plots in this paper are visualized by plotting one isosurface of the imaginary part of the complex eigenvalue of the velocity gradient tensor. The corresponding isosurface value, which is non-dimensionalized by f, is 16 for all of the vortex topology plots. In (*e,f*) we show one isosurface of pressure ($p/(0.5\rho U^2) = 1.1$) at $t/T = 0.25$ and 0.82, respectively.

flapping cycle takes $\sim$700 time steps. The simulations have been performed on 256 CPUs of Kraken, which is a Cray XT5 system and on this system, it takes $\sim$20 CPU hours to simulate one cycle. In the current work, each simulation was integrated over four flapping cycles. Estimates of cycle mean and r.m.s. lift as well as r.m.s. drag indicate that there is a less than a 1 % difference in these quantities from the third to the fourth cycle. Thus, the flow quantities reach a near-stationary state by the third cycle and all of the flow statistics in the following discussions are estimated based on averaging over the third and fourth cycles.

3.4. *Flow structure*

Figure 6(*a–d*) show the vortex structures around the body and wings of the hovering moth during one cycle. A distinct LEV is generated at the beginning of downstroke (see figure 6*a*). In addition, a tip vortex (TV) and a trailing-edge vortex (TEV) are also generated from each wing and these are observed to wrap around the wing.
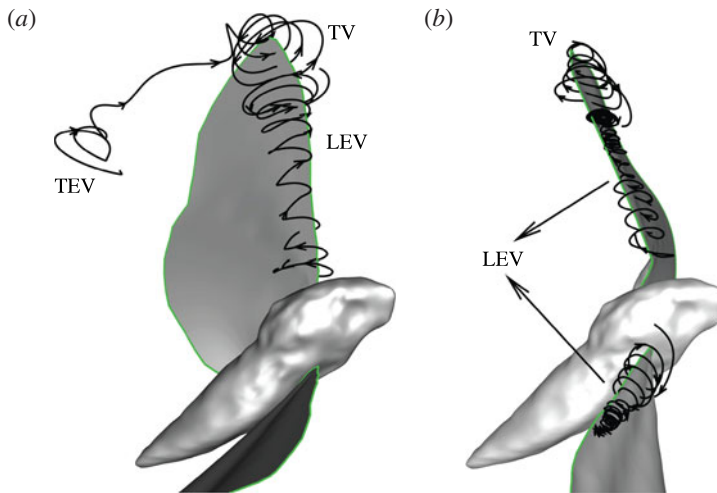
FIGURE 7. (Colour online) LEV and TV during (*a*) downstroke and (*b*) upstroke. The discontinuous arrows in (*a*) represents the flow direction along the vortex core.

Similar horseshoe-shaped vortex which comprises a LEV, a TV and a TEV was also reported by Liu & Aono (2009). Later, as the wings start to accelerate downward (figure 6*b*), the LEVs and TEVs grow in size and the TEVs are shed from the wings. The LEV covers a large part of the wing surface and accounts for the lift peak during downstroke; figure 6(*e*) show an isosurface of negative (suction) pressure at $t/T = 0.25$ and this clearly shows the large region of suction pressure on the top surface of the wing due to the strong LEV. During upstroke (figures 6*c* and 6*d*), the LEVs are much weaker than those during downstroke due to a reduced effective AoA of the leading edge and the corresponding suction pressure in figure 6(*f*) is significantly diminished.

Figure 7(*a*) shows the coherent LEV which stretches from the base to approximately 75 % of the wing length during mid-downstroke. A strong axial flow with a velocity of 50 % of average wing-tip velocity towards wing tip along the LEV core is observed in the current study during downstroke. The phenomenon was also noted in previous experiments (Ellington *et al.* 1996) and numerical simulations (Liu *et al.* 1998). Figure 7(*a*) also indicates a spiral TV with a axial flow towards the wing root. In contrast, during the upstroke, the LEV is much weaker due to a smaller AoA ($\sim 30°$ compared with 60° during the middle of downstroke), and the strength of the LEV decreases towards the wing tip. The TV is still strong during the upstroke, and this results in a low pressure at the wing tip as shown in figure 6(*f*).

3.5. *Force comparison*

Figure 8 shows a comparison of the time-varying vertical and horizontal forces obtained from the experiments as well as NS simulation; the corresponding mean values are given in table 1. The NS simulation was based on a cyclical repetition of the one synthesized flapping stroke. First, for the NS simulation, the average lift produced by the two wings is 14.9 mN and this matches reasonably well with the weight of the insect (13.6 mN). It should be noted that most past computational studies have limited their validation to this comparison (Liu & Aono 2009). However, since our interest here is to correctly predict not only mean values but also the time-varying variation of lift and drag, we have conducted a more extensive validation.

	Cycle mean		Cycle r.m.s.		Downstroke mean		Upstroke mean		Down/up	
	EXP	NS	EXP	NS	EXP	NS	EXP	NS	EXP	NS
Lift (mN)	15.0 ± 4.8	14.9	20.8 ± 5.3	20.6	22.3 ± 4.4	23.0	7.17 ± 4.4	8.19	3.11	2.81
Drag (mN)	0.56 ± 4.8	0.44	17.0 ± 5.2	20.9	15.4 ± 4.4	18.4	-12.2 ± 4.4	-17.2	1.27	1.07
Energy (mJ)		2.62				1.76		0.86		2.05
Power (mW)		66.1				97.1		39.7		2.45
η_p (N W^{-1})		0.23				0.24		0.21		1.14

TABLE 1. Comparison of lift and drag forces between NS simulation and experiment as well as energy and power related metrics computed from NS simulation. In the table, η_p refers to the power-loading which is the ratio of mean lift to power.

FIGURE 8. A comparison of the instantaneous vertical (*a*) and horizontal (*b*) force between the current NS simulation, the experimental results, and the previous simulations of Liu & Aono (2009).

Going beyond a comparison of mean values, figure 8(*a*) indicates that the time variation of the vertical force in the NS simulation is also in good agreement with the experimental result. The NS simulation accurately predicts the rise of the lift force during the initial phase of the downstroke as well as the peak lift value of $\sim$44 mN. The agreement between the two during the latter half of the downstroke is also quite good with the simulated value falling mostly within the variability of the experiments. The upstroke is found to produce less lift but the experimental variability is of the same magnitude as for the downstroke. In terms of the comparison, the NS simulation correctly indicates the presence of two small peaks in lift during the upstroke but over-predicts the lift at mid-upstroke. At all other phases during the upstroke, the computed values lie within the experimental uncertainty.

The match between NS and experiment is less precise for the horizontal forces, but the simulation does predict the key features of the overall time course reasonably well. First, the wings produce a drag force during downstroke and a thrust force during upstroke. The drag and thrust nearly cancel each other during one flapping cycle for the hawkmoth in hover in both the simulation and the experiment, with the mean horizontal force coming out to be $\sim$3 % of the mean lift force. This is in line with the fact that during hover, the net acceleration of the insect in the horizontal plane is expected to be negligible. The horizontal force peak during downstroke is sharper and larger than that during upstroke. This trend, which is due to the strong LEV formed in downstroke is also captured correctly in the simulation. The Pearson correlation coefficients (defined for two variables X and Y as $\gamma_{XY} = \text{cov}(X, Y)/\sigma_X \sigma_Y$ where cov and σ are the covariance and standard deviation, respectively) between simulation and experiment for the time-varying lift and drag are 0.93 and 0.90, respectively, which provide quantifiable confirmation of the match between the corresponding profiles.

Table 1 enables further quantitative comparison between the experiment and the simulation. The table includes estimates of experimental uncertainties; these are noted to be larger than those typical for controlled engineering experiments and are a manifestation of the inherent difficulty of conducting measurements of freely flying animals. The estimates have been broken down into upstroke and downstroke phases

as well as mean and r.m.s. quantities in order to provide a more nuanced and critical assessment of the comparison. We note that every single quantity from the simulation, except for the upstroke mean drag, falls within the experimentally measured range of values of the corresponding quantity. The cycle mean, cycle r.m.s. and downstroke mean of the lift from the simulations are in particularly good agreement with the experiment. As pointed out earlier, the drag-associated quantities do not show the same level of agreement. This is likely indicative of the fact that while weight support during hover requires the animal to generate a more consistent level of lift in every flapping cycle, horizontal forces are more variable from cycle to cycle so as to enable flight stabilization and other small adjustments to the lateral location of the animal. Finally, the ratio of mean lift produced during downstroke to that produced during upstroke is computed from NS modelling to be 2.81 and is estimated in experiments to be 3.11. This clearly shows dominant role that the downstroke plays in producing lift during hover. The comprehensive comparison of forces between simulations and experiments provides a high level of confidence regarding the fidelity and accuracy of the computational model.

As noted earlier, while past modelling studies have found a reasonable match between the computed mean lift value and the weight of the insect, no past study has validated the *time-varying* lift and drag with a corresponding experiment in a comprehensive manner. Figure 8 includes the lift and drag data extracted from the studies of Liu & Aono (2009) and Aono *et al.* (2009). In this previous work, the mean vertical force was 17.1 mN, which was 9 % higher than the reported weight of the hawkmoth. The mean drag force was reported to be less than 3 % of the mean vertical force and this is similar to the current study. Furthermore, we have estimated the r.m.s. values of lift and drag for this previous work to be 20.6 and 20.3 mN respectively, and these values match reasonably well with the current simulation. Compared with current model, the lift produced from this previous model is smaller between $t/T \sim 0.2$ and 0.3 and larger from $t/T \sim 0.3$ to 0.4. The lift peaks during upstroke for the current and previous models occur at different times. Furthermore, the lift peak during upstroke is significantly larger for the previous model than for the current model. Consequently, this previous model predicts a ratio of downstroke to upstroke lift that ranges between 1.5 and 2.3 compared with 2.81 for the current model.

These differences in force production between the two studies are likely connected with the differences in the wing kinematics. For example, during downstroke (t/T from 0.2 to 0.3), the wings flap downward with a higher AoA for the current model than that for the previous model. This could lead to a stronger LEV that results in a higher lift. For t/T from 0.3 to 0.4, the wings of the current model begins to decelerate and start to rotate, as indicated by the stroke angle in figure 4(*a*), while the wings of previous model continue a downward motion with a large AoA. Also, it can be seen that the first lift peak during upstroke for previous model is significantly larger than that for the current study. This may be explained by the significant ($\sim 20°$) wing twist in the current model during upstroke which is a manifestation of wing flexibility. It can be noted that the difference of AoA between the proximal and distal parts of the wing at $t/T \sim 0.7$ leads to a significant discrepancy in the angle between the wing chord and the horizontal plane. In the current model, this angle is much higher, especially at the proximal part of the wings, which results in a smaller vertical component (smaller lift peak for current model) of the aerodynamic force.

The simulations also allow us to estimate the power expended in producing the lift force by integrating the pressure and shear associated work on the surface of the wing. This quantity is an essential component of hovering efficiency but is not obtainable

directly from insect flight experiments. Note that power is obtained from a dot-product between the local time-varying aerodynamic force and wing velocity. Since we have matched the local wing velocity closely to experimental data and also demonstrated a reasonably accurate prediction of the time-varying forces on the wing, we can be reasonably assured that the aerodynamic power estimated from our computations is accurate. This is crucial since estimates of power form an essential starting point for the stroke optimization studies described later in the paper. Aerodynamic power associated quantities are also shown in table 1. We find that the moth uses ∼66 mW of power per cycle during hover. We compare this to experimental measurements of power expended in real moths by following Stevenson & Josephson (1990), estimating that 21 % of the hawkmoth's mass is flight muscle, giving a muscle mass-specific power of approximately 230 W kg^{-1}. This is substantially greater than estimates from early aerodynamic models (Willmott & Ellington 1997*b*) that predate the discovery of leading edge vortices in insect flight and also *in situ* flight muscle work-loop studies, both of which produce estimates from 90 to 130 W kg^{-1} (Stevenson & Josephson 1990; Tu & Daniel 2004). However, our results are consistent with the measured oxygen consumption of hovering Manduca of 12.2 ml O$_2$ kg^{-1}, which at 20 % muscle efficiency and 20 % flight muscle mass fraction also implies a power output of 230 W kg^{-1} (Casey 1976).

This 66 mW mean power per cycle leads to a power-loading (η_p), which is the ratio of lift produced to the aerodynamic power expended by the wing, of 0.23 N W^{-1}. Estimates of power-loading for up and downstrokes indicate that even through lower lift production in the upstroke is associated with lower power consumption, the power loading of the upstroke is ∼13 % lower than that of the downstroke. This clearly indicates the potential for improving upon the power efficiency of the hawkmoth stroke and finding stroke kinematics that are power-optimized for hover. This aspect is addressed in the following section.

4. Stroke optimization of hawkmoth-inspired flapping wings

As described earlier, the hawkmoth may not have the optimal wing stroke for a given MAV design criteria and thus, strategies for improving on its performance are desirable. We use a multi-fidelity approach where we explore a parameter space and apply numerical optimization strategies with the BEM, and assess the true performance of candidate strokes identified by the BEM using the NS model. We also constrain our search for improved flapping kinematics to cases that fit within the existing kinematic envelope of the moth. For instance, increasing the size of the wings while holding all other parameters constant could improve the lift generating capability of the moth, but would not demonstrate meaningful optimization. Similarly, increasing the flapping amplitude or frequency could also lead to force increases but would not allow us to understand the optimality of the hawkmoth wing-stroke. Thus, we restrict our optimization to use the same wing and overall flapping frequency and amplitude as the actual moth.

4.1. *Parametrization of wing kinematics*

An initial requirement for such an approach is a reduction in the complexity of wing motions to a manageable set of parameters which can be varied systematically. Here, we specify the trajectory of the moth's wing tip as a simple harmonic motion and use a hypertangent-based function to describe the spanwise rotation of the wing. A simple harmonic motion approximation of the flapping kinematics was chosen as the simplest

Parameter	Value (rad.)
ϕ_A	0.297
$\bar{\phi}$	0.007
δ_ϕ	0
θ_A	0.815
$\bar{\theta}$	−0.012
δ_θ	0.641
α_A	0.975
$\bar{\alpha}$	1.294
δ_α	2.268
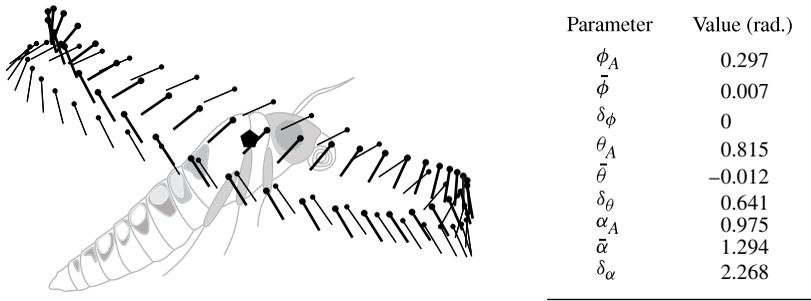
FIGURE 9. A lateral projection of the actual (heavy black lines with filled circle) and simple harmonic motion (light black lines with filled circle) wing kinematics recorded from the hovering hawkmoth. Wing position and orientation is shown with circle/diamond at the leading edge and a line showing wing orientation. The wing root is shown on the moth body as a black pentagon. The wing moves in a clockwise manner, with the downstroke trajectory passing above the wing root and the upstroke below it. The wing chord length shown is one-quarter of the actual mean chord length to enhance figure visibility. The parameters are those for the simple harmonic motion equation (4.1)–(4.3). Note that the best-fit simple-harmonic-motion-based kinematics matches the actual wing kinematics better in the downstroke than the upstroke. This is a compromise that has to be made in order to retain a simple kinematic prescription for the optimization study.

means for describing oscillatory wing motion and to simplify the extraction of the coefficients from real animal data via Fourier analysis. These parameterized motions are given by

$$\phi_i = \phi_A \sin(2\pi\hat{t} + \delta_\phi) + \bar{\phi} \tag{4.1}$$

$$\theta_i = \theta_A \sin(2\pi\hat{t} + \delta_\theta) + \bar{\theta} \tag{4.2}$$

$$\alpha_i = \alpha_A \tanh(\pi/2 \sin(2\pi\hat{t} + \delta_\alpha)) + \bar{\alpha} \tag{4.3}$$

where ϕ_i is the elevation angle at non-dimensional time t/T of $\hat{t}$, with ϕ_A being its amplitude, $\bar{\phi}$ its mean and δ_ϕ its phase. The sweep angle θ_i is also specified by its amplitude θ_A, mean $\bar{\theta}$ and phase δ_θ. Spanwise rotation α_i has an amplitude α_A, a phase δ_α and a mean $\bar{\alpha}$. Note that these equations describe wing motion in a body coordinate frame $X'Y'Z'$ and not in the global or stroke-plane frames.

Figure 9 shows a comparison of the actual hawkmoth flapping kinematics with the 'best-fit' approximation using (4.1)–(4.3), and the adjoining table shows the kinematic parameters for this best-fit stroke. For the purposes of parameter exploration and optimization, we consider this stroke to be the baseline case.

4.2. *Blade-element tuning based on the NS simulation*

Prior to using the BEM as either a parameter-space exploration tool or for numeric optimization, the BEM coefficients are 'tuned' or calibrated to the NS results by running the NS simulation with a rigid wing and flapping parameters similar to those shown in figure 9. The same wing planform and kinematic parameters are then modelled using BEM, and the BEM coefficients varied from values presented in Hedrick & Daniel (2006) to minimize the mean-square difference in the time-varying lift and drag reported by the NS simulation. The resulting tuned value for C_{rot}
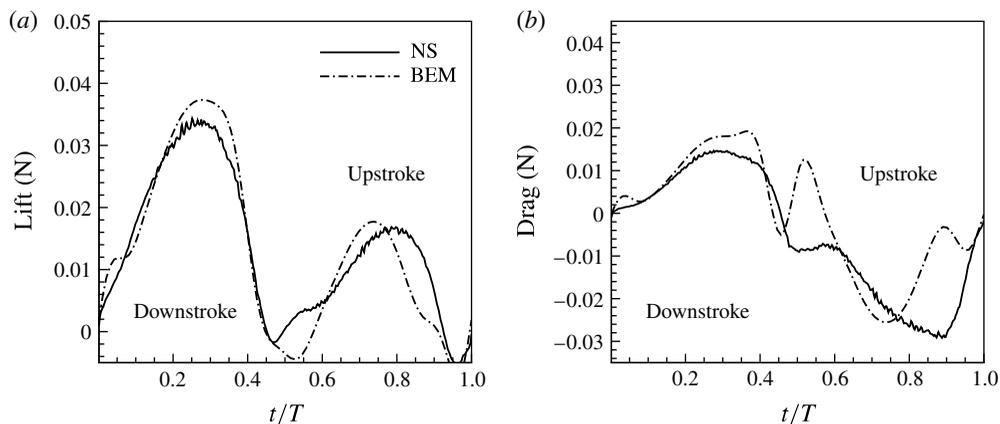
FIGURE 10. Lift (*a*) and drag (*b*) comparison between NS simulation and BEM for baseline case. Note that the BEM was tuned by the results from NS simulation.

$(\delta_\theta, \delta_\alpha)$	Baseline case (−10, 0)		High-lift case (−30, −30)		High-η_p case (20, 10)	
	BE	NS	BE	NS	BE	NS
Lift (mN)	12.9	13.5	13.8	11.7	12.5	10.2
Power (mW)	60.7	48.7	61.8	41.3	52.5	38.3
η_p (N W^{-1})	0.21	0.28	0.22	0.28	0.24	0.27

TABLE 2. Mean values of lift, power and power loading expended during one cycle, downstroke and upstroke from BEM and NS simulation.

(equation (2.3)) was 0.55, and the tuned C_{trans} (equation (2.2)) is given by

$$C_{trans} = [(1.3 \sin(2\alpha' + 0.30) + 0.4 \cos(\alpha' - 0.59) + 0.01)^2$$
$$+ (1.3 \sin(2\alpha' - 0.70) + 0.3 \cos(\alpha' - 1.33) + 1.60)^2]^{1/2} \quad (4.4)$$

where α' is the instantaneous angle of incidence of the strip on the wing relative to local incoming flow.

The resulting match between BEM and NS simulation for identical wings and kinematics is shown in figure 10. The BEM lift is a better match to its NS counterpart than BEM drag, and both BEM lift and drag tend to match the NS output better in the early to middle portions of downstroke and upstroke. Furthermore, the mean lift, which is shown in table 2, indicates a 4.4 % difference between NS and BEM. The general effect of this tuning on the original BEM with coefficients drawn from studies of insect flight based on mechanical flappers (Dickinson *et al.* 1999; Usherwood & Ellington 2002; Sane 2003) is to reduce the forces due to wing rotation (equation (2.3)) and wing translation (equation (2.2)) to approximately 52 and 95 %, respectively, of their original magnitude as given in Hedrick & Daniel (2006). The use of a flat-plate wing with no spanwise or chordwise curvature and the adoption of a sinusoidal motion with the additional constraints on frequency and amplitude that we have prescribed here results in an overall reduction in mean lift to 13.5 mN and an
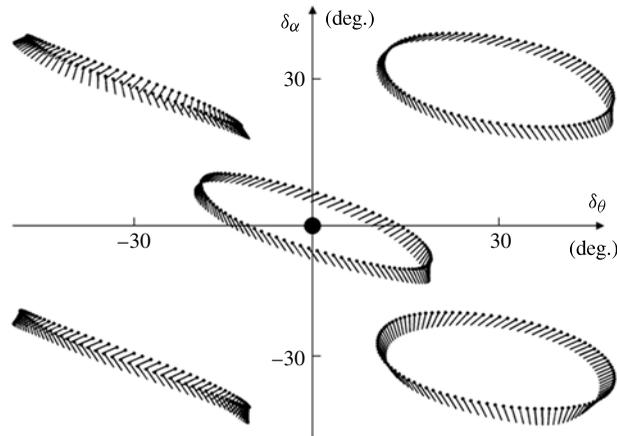
FIGURE 11. Wing trajectory of some selected cases in the optimization exercise I. As before, wing position and orientation is shown with circle at the leading edge and a line showing wing-chord orientation.

increase in power loading to 0.28, respectively, which represents a 9.4 % reduction and a 21.7 % increase in these two quantities, respectively. Notwithstanding the difference in the performance from the actual hawkmoth kinematics, we consider this case to be the baseline for the optimization studies.

4.3. *Optimization exercise I*

The multi-fidelity optimization assumes that the BEM provides reasonably accurate estimates of key quantities such as lift, drag and power in the parametric vicinity of the baseline case for which it is tuned. If this assumption is borne out, then the BEM can be used to search the parametric space for optimal solutions and a NS model employed to more accurately assess the performance of select cases. Assessing the validity of this assumption is a key component of this section but before that, we present the results of the BEM-based parameter search and identify strokes that may be considered high-performing. We systematically varied the timing of wing horizontal motion and wing spanwise axis rotation, changing δ_θ and δ_α, respectively, in the range of -30 to $+30°$ about $(\delta_\theta, \delta_\alpha) = (0.0, 0.0)$. The first of these parameters changes the profile of the stroke from a narrow, tilted ellipse to a more circular profile and the second changes the angle of incidence throughout the stroke as is shown in figure 11. These parameters were selected because the BEM predicts that they influence the magnitude of flight forces without changing the overall flapping amplitude or frequency. In contrast, changes to the BEM flapping amplitude parameters ϕ_A and θ_A also influence force production, as is expected under simple, analytic models of flapping flight (Weis-Fogh 1973) but are less interesting to explore in the current context. Note that in the current study, δ_ϕ is kept at a value of zero and this provides a distinct datum for the other phase angles.

The wing trajectories of five sample cases are shown in figure 11. Note that even the variation of just these two parameters produces a wide variety of wing strokes. While this enhances the possibility that strokes with higher performance might be identified, it also presents a challenge for BEM-based prediction, which was originally developed using parameters near those used by actual hawkmoths and may not extrapolate well to more unusual wing strokes.
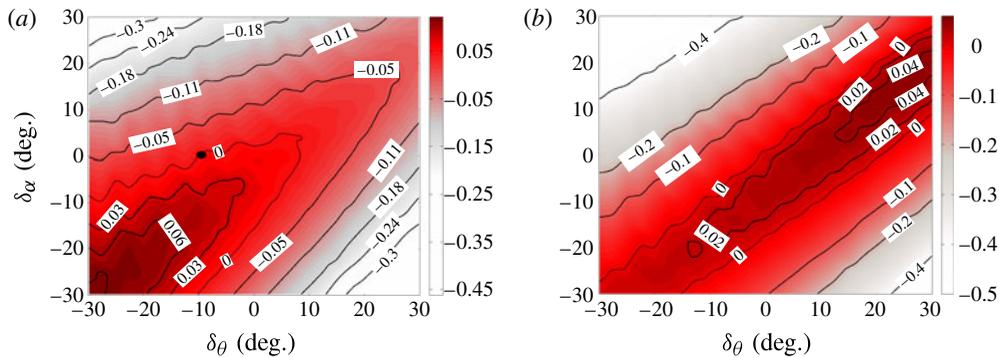
FIGURE 12. (Colour online) Performance map from BEM showing mean (*a*) lift and (*b*) power loading with the two phase-offset angles. The values showed in the plots are the relative difference with the baseline case (identified by a black dot). The dashed curves show the cases that can produce the same lift and power loading as the baseline case. Positive (negative) contour values indicate an increase (decrease) over the baseline value; dark shades indicate the highest increases.

4.3.1. *BEM simulations and predictions*

Parameter mapping with the BEM was conducted over a grid of $\triangle\delta_\theta$ and $\triangle\delta_\alpha$ ranging from $-30°$ to $30°$ with a $2.5°$ spacing which adds up to a total of 576 cases, and figure 12 shows the relative change (over the baseline case) of the mean lift and power-loading for all these cases. The following observations can be made from these BEM-based performance maps.

(*a*) The baseline case is neither optimal in terms of lift nor power loading since there are many other cases which seem to provide better performance in these metrics than the baseline case.

(*b*) Local maxima in lift and power loading seems to exist thereby reaffirming that even within the severe constraints imposed here, it may be possible to find 'optimal' strokes. The performance gains however seem to be marginal: a 7 % increase in lift and a 12.5 % increase in power loading over the baseline case.

(*c*) The strokes for high lift and high power loading are far apart in parametric space; high lift occurs for large negative values of the two phase offsets whereas high power loading occurs for large positive values of these two offsets. The strokes for high lift and high power loading look similar to the cases shown in the lower left and upper right corners in figure 11, respectively. From the point of view of MAV design and operation, this is not desirable since it requires a large kinematic range and variation in two parameters to access both these regimes. However, it should be noted that this particular behaviour is connected with the two parameters chosen here, and there might exist other parameter pairs that lead to a better confluence between high lift and high power loading.

(*d*) The mean lift and power of the baseline case estimated by BEM is 12.9 mN and 60.7 mW, respectively, which results in a power loading of only 0.21. While many strokes exceed the lift and power-loading of the baseline case, the BEM modelling also indicates that many strokes in this parameter space produce sufficient lift to support the weight of the moth (the line with 0.05 in figure 12*a*) and power loading that is larger than the actual moth model, which is 0.23 (the line with 0.08 in figure 12*b*) calculated by NS simulation. However, the contour plots also
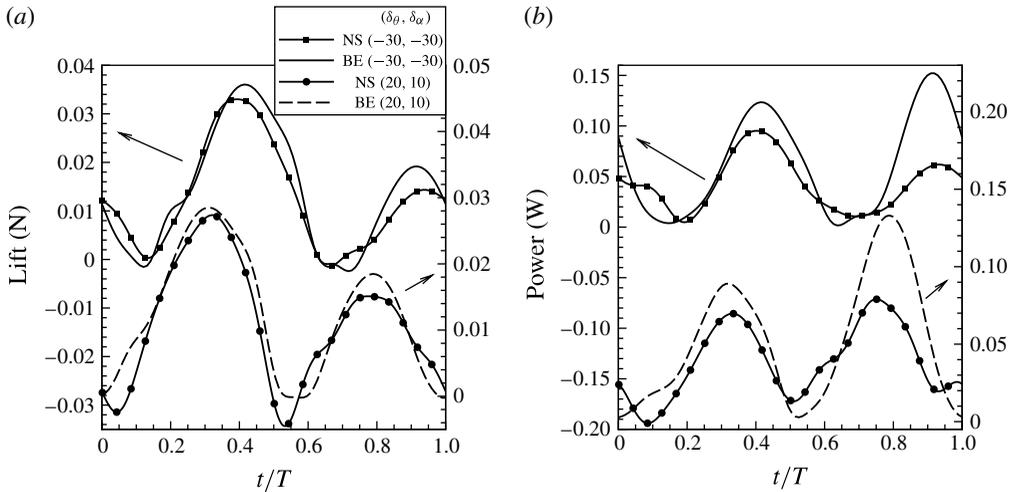
FIGURE 13. Lift (*a*) and power (*b*) comparison for cases with high lift ($(\delta_\theta, \delta_\alpha) = (-30, -30)$) and high power loading ($(\delta_\theta, \delta_\alpha) = (20, 10)$) estimated by BEM and NS models.

indicate that no case can produce sufficient lift to support the body weight while achieving higher power loading than the actual moth model.

4.3.2. *Evaluation of BEM prediction*

The caveat in all of the above observations is that they assume that the BEM can provide a fairly good estimate of the magnitudes and trend of these quantities in the vicinity of the baseline case and we now evaluate this assumption using NS modelling. First, figure 13 shows the time variation of lift and power for the two cases which correspond to the cases with high lift ($(\delta_\theta, \delta_\alpha) = (-30, -30)$) and high power loading ($(\delta_\theta, \delta_\alpha) = (20, 10)$), respectively, predicted by the BEM and table 2 shows the corresponding averaged values of lift, power and power loading for these cases both from BEM and NS; also included in the table are the values of baseline case for these two models. It can be seen from figure 13 as well as the table that while the lift matches reasonably well between BEM and NS, BEM significantly overestimates the magnitude of the power. In particular, figure 13 shows that overestimation of power is primarily during the upstroke. Table 2 also shows that the case identified as having high lift by BEM in fact has a lower lift than the baseline case; similarly, the case identified by the BEM as having high power loading actually has a power loading which is slightly lower than the other two cases as predicted by NS modelling.

The above mismatch between BEM and NS seems quite significant, especially for the power and power loading, but the possibility exists that the mismatch may be associated with the two cases with high lift and power loading being quite distant in parameter space from baseline case, which the BEM has been tuned from. To explore the extent to which BEM correctly predicts the magnitude and trend of aerodynamic quantities in this parameter space, we have conducted a series of NS simulations of cases for comparison with the BEM predictions.

Since it is not practical to conduct 576 NS simulations of a three-dimensional flapping wing, we have conducted a more limited subset (22 in total) of such simulations which are identified in the parameter space in figure 14. The contour plots of various quantities (figure 14*a*,*b*) for the NS simulations are generated by
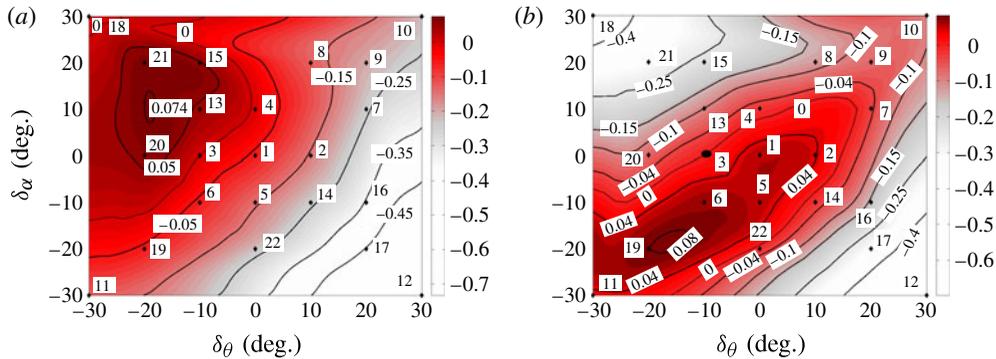
FIGURE 14. (Colour online) Performance map from NS modelling showing variation of lift (*a*) and power loading (*b*) with the two phase-offset angles. The values showed in the plots are the relative difference with the baseline case (identified by a black dot). The dashed curves show the cases that can produce the same lift and power loading as the baseline case. Positive (negative) contour values indicate an increase (decrease) over the baseline value; dark shades indicate the highest increases.

employing a cubic-spline data interpolation between these 22 cases. We focus here on comparing key aerodynamic quantities: lift and power loading, and the following observations can be made regarding this comparison.

(*a*) Within the parameter space explored, the NS model also predict a maximum in mean lift. However, the location of this maximum value in the parametric space is quite different from that predicted by the BEM; for the NS simulations the maximum occurs at around $((\delta_\theta, \delta_\alpha) = (-20, 10))$, while for the BEM, it occurs at around $((\delta_\theta, \delta_\alpha) = (-30, -30))$. Interestingly, the magnitude of the peak mean lift is $\sim 8\%$ higher than the baseline case and this is similar to the increase of 7% predicted by BEM. Thus, the magnitude of lift enhancement predicted by the two approaches is well matched while the overall trend is not.

(*b*) The NS simulations also indicate a local maximum in power-loading but in contrast to BEM, the peak in power loading is centred around $((\delta_\theta, \delta_\alpha) = (-15, -20))$. Furthermore, the NS simulations predict a peak in power loading that is $\sim 8\%$ higher than the baseline case whereas BEM predicts a 12.5% increase in this value. While this match in magnitude is not as good as that for the lift, it is nevertheless reasonable. It should be noted that there is also some similarity in the variation of power loading predicted by the two models in that the peak values of this quantity occur roughly along the diagonal (from lower left to upper right corner) of the parameter space. This closer match of the trend in this quantity could possibly be due to the fact that power loading is a ratio of lift to power and while lift and power trends are individually not well predicted by BEM, the differences in these two quantities are reasonably well correlated and cancel out to some extent in the estimation of the power loading.

(*c*) For the parameters spanned here, the region of high lift and high power loading do not coincide. There does not seem to be a region in this parametric space where both the lift and power loading exceed those for the baseline case 3. However, according to the NS simulations, with the elevation phase offset fixed at $-20°$, the wings can transition between high lift and high power loading by varying just the wing spanwise rotation phase offset. Table 3 shows stroke-averaged lift, power and
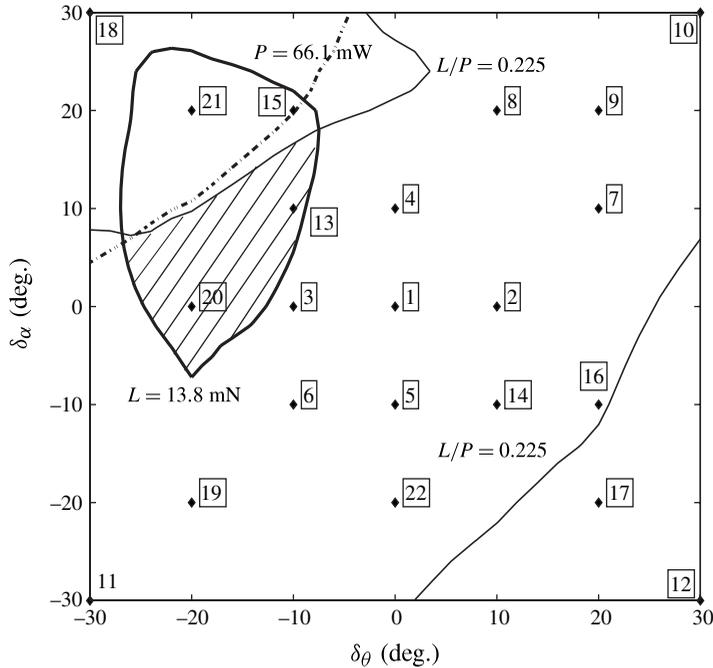
FIGURE 15. Performance map from NS modelling identifying particular regimes in lift and power measures that match the performance for the actual moth.

	Case		
	No. 19	No. 20	No. 21
$(\delta_\theta, \delta_\alpha)$	$(-20, -20)$	$(-20, 00)$	$(-20, 20)$
Lift (mN)	12.5	14.1	14.3
Power (mW)	42.2	55.5	75.7
η_p (N W^{-1})	0.30	0.25	0.19

TABLE 3. Mean aerodynamic quantities computed from the NS simulations for selected cases.

power loading for some selected stokes with elevation phase offset fixed at $-20°$; stroke no. 19 is a stroke with the highest power loading; stroke no. 20 lies inside the hatched region (see figure 15) and therefore has high lift and power loading; stroke no. 21 has high lift but low power loading. This is potentially a favourable feature from the point of view of MAV design and operation since it implies that just one degree of freedom in actuation could be used to transition between high-lift and high-power-loading regimes.

(d) The heavy solid contour in figure 15 corresponds to the weight of the moth (13.8 mN) and all of the cases that lie inside this closed contour produce lift that exceeds that needed to support the weight of the moth. The dash-dotted contour corresponds to power consumption equal to that of the actual moth from NS

	Mean lift	Mean power	Mean η_p	r.m.s. lift	r.m.s. drag
γ_{BEM-NS}	0.79	0.91	0.96	0.97	0.79

TABLE 4. Pearson correlation coefficient γ_{BEM-NS} between results from BEM and NS for force- and power-related quantities.

simulation, and all of the cases below this line consume less power than this value. The light solid contours corresponds to the power loading of the actual moth and all of the cases between these two contours exhibit higher power loading than this. Thus, the hatched region represents cases that exceed the body weight as well as the power loading of the moth and require power equal to or lower than that expended by the moth. Thus, even this highly restrictive parameter search produces wing strokes for hover that are aerodynamically superior to that of the moth. This also suggests that a more extensive search over a wider parameter space could possibly lead to strokes that more significantly outperform that of the moth and this is the subject of the next section.

(*e*) Many of the qualitative observations made above regarding the match between BEM and NS simulations are confirmed quantitatively by computing the Pearson correlation between the results of the 22 NS simulations and the corresponding BEM predictions. Table 4 shows these correlations for mean lift, power and power loading, factors which are essential to the aerodynamic performance. The table also includes correlation for the r.m.s. lift and drag, and these go beyond mean-value comparisons to provide an assessment of the match in the temporal variability of these two quantities. Overall, the correlations for the mean values range from 0.79 to 0.96 and those for the r.m.s. values between 0.79 and 0.97 indicating that the BEM is able to predict the trends in all of these quantities quite well. Interestingly, as noted earlier, the correlation in power loading is higher than that of mean lift or power; this observation works in the favour of using BEM as part of a multi-fidelity modelling tool for optimizing stroke aerodynamics in flapping flight.

4.3.3. *Predictive limits of BEM*

Although the match between BEM and NS is shown to be reasonably good, the availability of NS simulation data provides an opportunity to further explore and understand the limits of BEM as applied to such flows. Figure 16 shows the relative difference of cycle-averaged lift between BEM and NS models over the parameter space explored in both approaches. It is noted that isolines of this quantity are generally inclined along the diagonal from bottom left to top right. This suggests that the relative accuracy of the BEM prediction is maintained as long as the phase difference between translation (represented by sweep angle θ) and spanwise rotation (represented by rotational angle α) is kept the same. Conversely, the prediction from the BEM deteriorates rapidly if the relative phase between these two is changed. Note that along the diagonal line (the line connecting cases 11 and 10), the phase difference between rotational angle and sweep angle is zero, which implies the rotation is precisely in phase with stroke reversal; figure 17(*a*) shows the wing kinematics for case 19 which is representative of these cases. For cases above this line, wing rotation
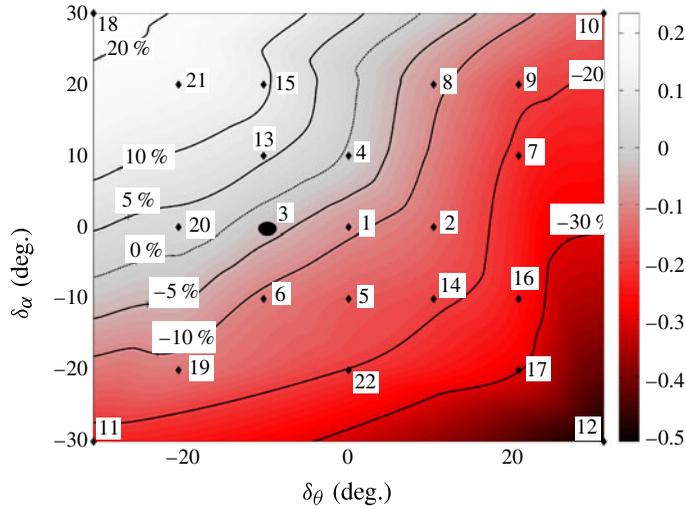
FIGURE 16. (Colour online) Performance map showing the relative lift difference between BEM and NS modelling. The dashed curve shows the two methods predict the same amount of lift.
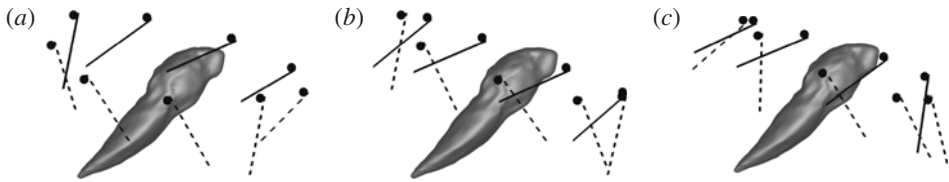
FIGURE 17. Wing kinematics for: (*a*) case 19, in which case the rotation occurs symmetrically with the stroke reversal; (*b*) case 21, in which case the rotation is prior to stroke reversal; and (*c*) case 17, in which case the rotation is delayed. The dots in the plots indicate the leading edge dashed and solid lines denote upstroke and downstroke, respectively.

precedes stroke reversal (see figure 17*b* for case 21), while for cases below this line, the rotation occurs after stroke reversal (see figure 17*c* for case 17).

In order to understand the flow physics underlying the trend observed in figure 16 we examine the vortex structures for a few selected cases. In figure 18 are shown the flow structures produced by the baseline cases 3 and 8, which, although separated by 20° phase in both δ_θ and δ_α with respect to the phase of the elevation angle, maintain the same phase relative to each other. An idea of the difference in the two wing trajectories can be gleaned from figure 11. Despite the significant difference in wing kinematics, figure 18 shows that the vortex structures produced by the two are very similar; for both cases, an LEV is generated during early downstroke (a1 and e1 in figure 18*a,e* respectively). This LEV later grows towards the wing root until it spans the entire leading edge of the wing during mid-downstroke (figure 18*b,f*) and mid-upstroke (figure 18*d,h*). Similar LEVs are also generated for the two cases during the upstroke (figure 18*c,g*).

The similarity in the vortex structures noted above can be contrasted to cases 17 and 19, examples where the phase angles δ_θ and δ_α change relative to one another as
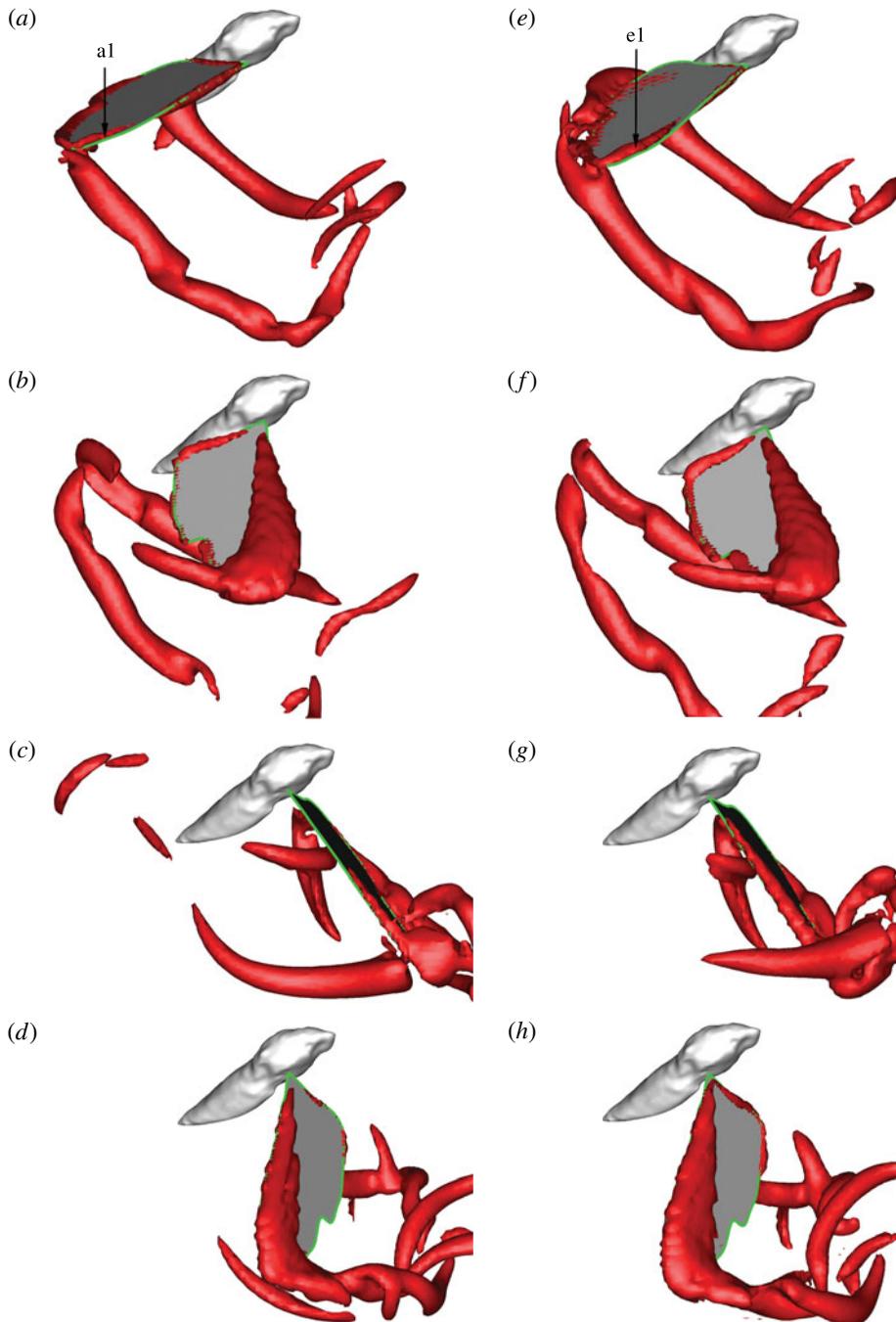
FIGURE 18. (Colour online) Vortex structures for case 3 ($a \sim d$) and case 8 ($e \sim h$) at: (a,e) $t/T = 0.1$; (b,f) $t/T = 0.25$; (c,g) $t/T = 0.53$; and (d,h) $t/T = 0.82$. All of the three-dimensional vortex topology plots in this paper are visualized by plotting one isosurface of the imaginary part of the complex eigenvalue of the velocity gradient tensor. The corresponding isosurface value, which is non-dimensionalized by f, is 16 for all of the vortex topology plots.
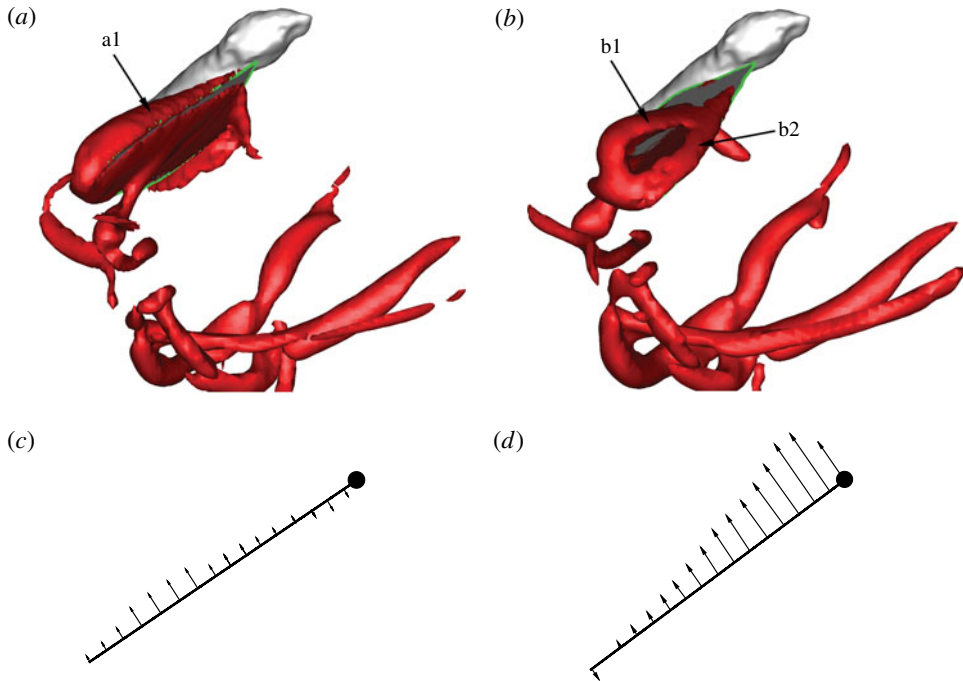
FIGURE 19. (Colour online) Vortex structures during early downstroke for case 17: (*a*) $t/T = 0.05$; (*b*) $t/T = 0.1$. Aerodynamic traction vectors on wing surface at 2/3 span: (*c*) case 3 at $t/T = 0.1$; (*d*) case 17 at $t/T = 0.1$.

well as with respect to the overall stroke timing. Figure 19 shows the flow structures produced by the wing in case 17 during early downstroke. As is shown in figure 17(*c*), at the beginning of downstroke the wing flaps downward and rotates rapidly at the same time, which leads to a very strong LEV (see a1 in figure 19*a*). Compared with the developing LEV shown in figure 18 (a1 in *a* and b1 in *e*) for cases 3 and 8, the LEV produced by the case 17 wing is significantly stronger and is even detached (see b1 in figure 19*b*) from the leading edge of the wing. The surface traction vectors shown in figure 19(*c*,*d*) show that the stronger LEV for case 17, produces a larger leading-edge suction.

Figure 20 shows a comparison of vortex structures at the beginning of downstroke for cases 3 and 21. The LEV produced in the immediately preceding upstroke is already shed from the leading edge in case 3 (see a1 in figure 20*a*), while it remains attached due to the rapid rotation at the end of upstroke for case 21 (see b1 in figure 20*b*). This attached vortex is 'captured' during the downstroke by the wing and influences the aerodynamic forces as shown in the comparison of corresponding surface traction vectors in figure 20(*c*,*d*). These new phenomena of LEV detachment (see figure 19) and vortex capture (see figure 20) and the associated force changes cannot be predicted by the current BEM since it has been tuned for a case that does not have these flow features. More extensive 'tuning' of the BEM force coefficients and perhaps even improved models that allow for additional flow phenomena might further enhance the effectiveness of the multi-fidelity approach.
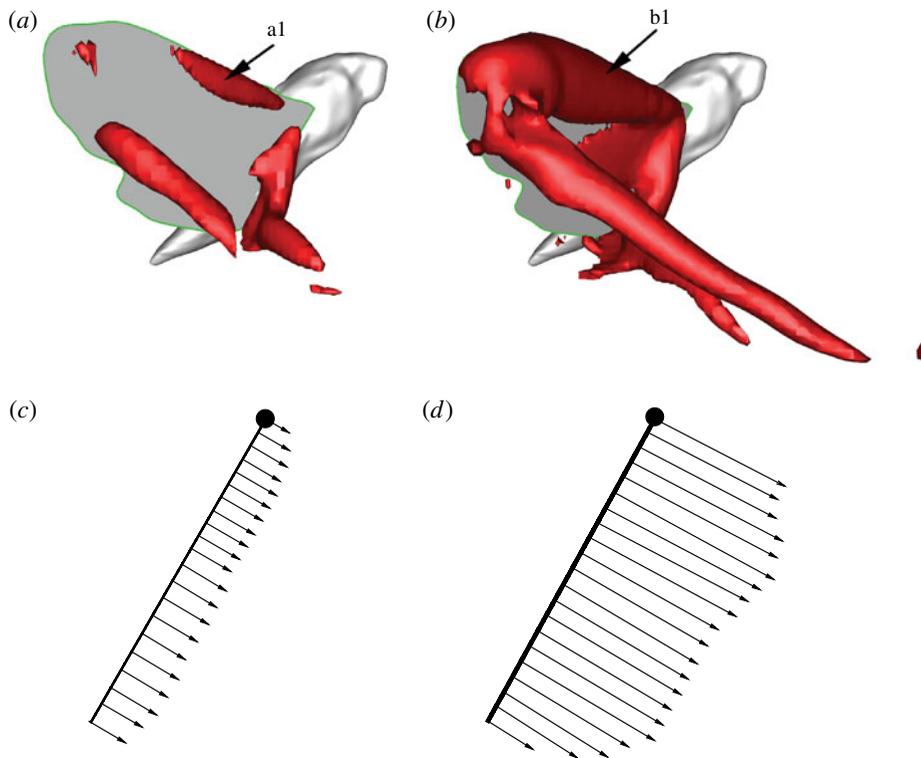
FIGURE 20. (Colour online) Vortex structures at the very beginning of downstroke: (*a*) case 3 at $t/T = 0.015$; (*b*) case 21 at $t/T = 0.015$. Aerodynamic traction vectors on wing surface at 2/3 span: (*c*) case 3 at $t/T = 0.015$; (*d*) case 21 at $t/T = 0.015$.

4.4. *Optimization exercise II*

While biological flyers such as the hawkmoth examined here are the product of millions of years of evolution, this does not necessarily result in optimal flight performance from the viewpoint of an engineered system designed for a specific application. Even setting aside biological limitations on available power and material properties that limit the flapping frequencies, amplitudes and wing sizes of animals, the hawkmoth may not necessarily use energetically optimal wing kinematics in hovering flight. For instance, the moth may use flapping kinematics that enhance maneuverability or stability at the expense of efficiency, or require fewer degrees of freedom at the wing base to produce. Our initial parameter mapping exercise, designed to explore the combined use of the BEM and NS approach for flight optimization, revealed that: (*a*) even in a highly restricted parameter space, a number of cases offer greater force and/or power loading than that of the actual moth; (*b*) overall magnitudes of lift are reasonably well predicted by a suitably tuned BEM; and (*c*) trends in power loading are better predicted than those for lift.

These above three observations suggest a path forward for determining strokes that are significantly superior in terms of aerodynamic performance than the moth. Here we use the GA (Krishnakumar 1989) and a simplex search (Nelder & Mead 1965) framework coupled with the BEM modelling approach to find wing kinematics which outperform the actual moth as assessed by the power loading; we then assess and

verify the aerodynamic performance of this stroke using NS simulations. Unlike the previous optimization exercise, we loosen the constraints on the kinematics; we allow the BEM-based optimizer to search over a large region of the parameter space defined by (4.1)–(4.3) for a stroke that maximizes power loading. The following constraints are imposed on the search.

(*a*) The overall flapping frequency and flapping amplitude is constrained to be similar to that of the actual moth. Although changes to these parameters may improve performance, there is no guarantee that they do not involve costs not measured in the simulation, such as the additional inertial power requirements.

(*b*) We require that the lift equals the body weight of the moth. Even though we know that BEM might not produce the correct magnitude of lift, the constraint on lift ensures that the subset of solutions considered produce acceptable realistic levels of lift.

(*c*) We also require that the strokes produce no net pitching moment. This constraint on moment guarantees that strokes that significantly modify the stability characteristics of the animal are deemphasized in the search.

This search, the result of 10^5 cost function evaluations, structured as 1000 generations of 100 individuals each in the GA and followed by an additional 10^4 cost function evaluations in the simplex search, results in the wing kinematics that are depicted and tabulated in figure 21. Compared with the actual moth kinematics shown in figure 9, the optimized kinematics has a more horizontal stroke plane, represented in the blade-element parameters by an elevation amplitude ϕ_A which is nearly zero. The optimized flapping kinematics also has a slightly increased spanwise rotation amplitude α_A and sweep amplitude θ_A compared with the biologically derived parameters. The role of this increased spanwise rotation amplitude is to bring the wing closer in orientation to the horizontal plane at mid-upstroke and mid-downstroke and in the BEM computation, this reduces the magnitude of both lift and drag. Thus, interestingly, the optimization produced a condition close to normal hover which has been studied extensively in past studies (Ellington 1984; Liu & Aono 2009; Du & Sun 2010).

This blade-element flapping kinematics which is identified as optimal by BEM is assessed using NS modelling and the vortex structures associated with this stroke are shown in figure 21. Unlike the actual moth and other optimized cases in optimization exercise I, both half-strokes now produce similar LEVs due to the nearly horizontal stroke plane as well as the near symmetry of the two half-strokes. The suction pressure corresponding to the two LEVs during the two half-strokes are also quite comparable (see figure 21*b*,*c*). Comparing the instantaneous NS lift and power during a single flapping cycle for the actual moth and this optimized case (figure 22), the flapping kinematic with the horizontal stroke plane produces a smaller lift peak during downstroke and higher lift during upstroke. From both NS simulation and BEM, the magnitude of two peaks for the optimized case is nearly similar, however, BEM over-estimates the magnitude of both lift peaks. The optimized model in exercise II produces a lift of 14.8 mN, which is sufficient to support the weight of the insect. The power loading for this optimized model is 0.30, which is ∼33 % higher than that of the actual moth. In fact, the optimized model identified here outperforms all of the cases in optimization exercise I as well.

The significant increase in aerodynamic efficiency of this optimal stroke over the natural stroke of the moth raises a number of issues regarding biological and bioinspired flapping flight. Why has the hawkmoth, for which hovering is an important

(*a*)

Parameter	Value (rad.)
ϕ_A	-0.025
$\bar{\phi}$	-0.072
δ_ϕ	0
θ_A	1.056
$\bar{\theta}$	-0.140
δ_θ	0.140
α_A	1.126
$\bar{\alpha}$	1.524
δ_α	1.670

(*b*)

(*c*)
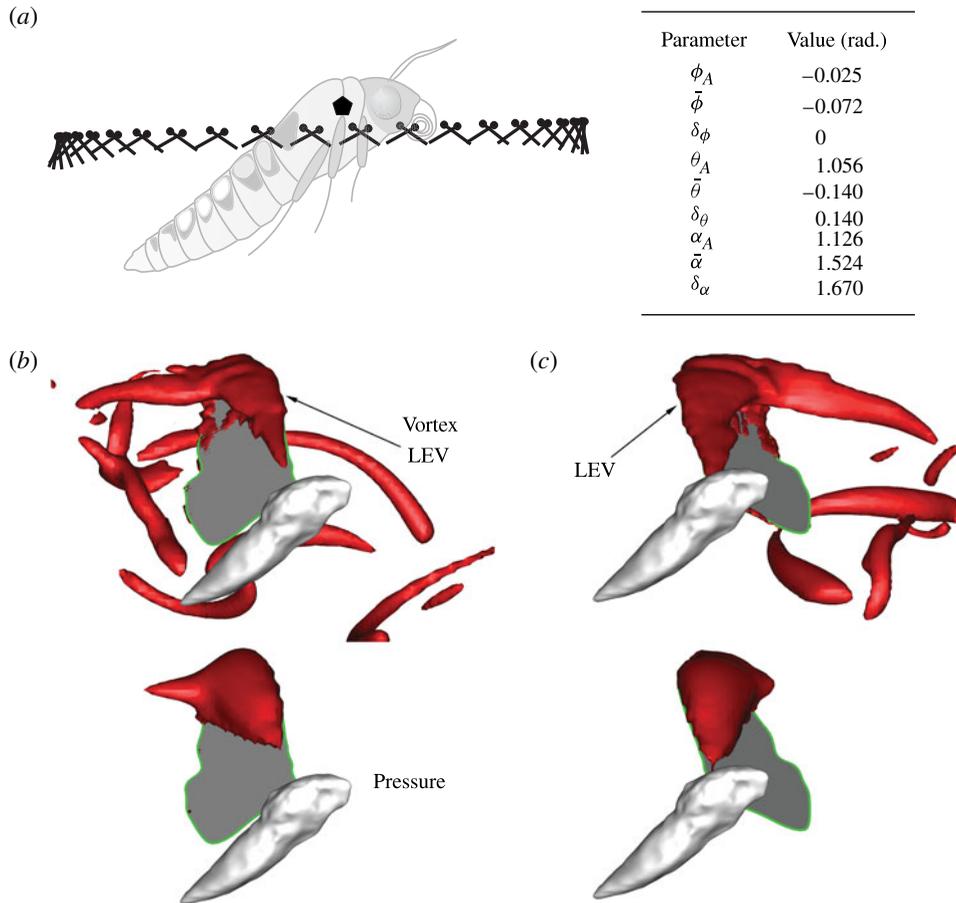
FIGURE 21. (Colour online) (*a*) A lateral projection of the optimized moth flapping stroke with a horizontal stroke plane. Wing position and orientation is shown with a dot at the leading edge and a line showing wing orientation. The wing root is shown on the moth body as a black pentagon. The wing chord length shown is one-quarter of the actual mean chord length to enhance figure visibility. The parameters are those for the simple harmonic motion equations (4.1)–(4.3). In (*b,c*) we show the vortex structures and the isosurface of non-dimensional suction pressure corresponding to a value of 1.1, respectively, at mid-downstroke and mid-upstroke for the optimized model.

	Cycle		Downstroke		Upstroke	
	BEM	NS	BEM	NS	BEM	NS
Lift (mN)	16.2	14.8	14.1	14.3	18.3	15.3
Power (mW)	57.5	49.2	61.8	57.0	53.2	41.3
η_p (N W^{-1})	0.28	0.30	0.23	0.25	0.35	0.37

TABLE 5. Mean values of power, power loading and energy expended during one cycle, downstroke and upstroke from NS simulation of the actual moth model.
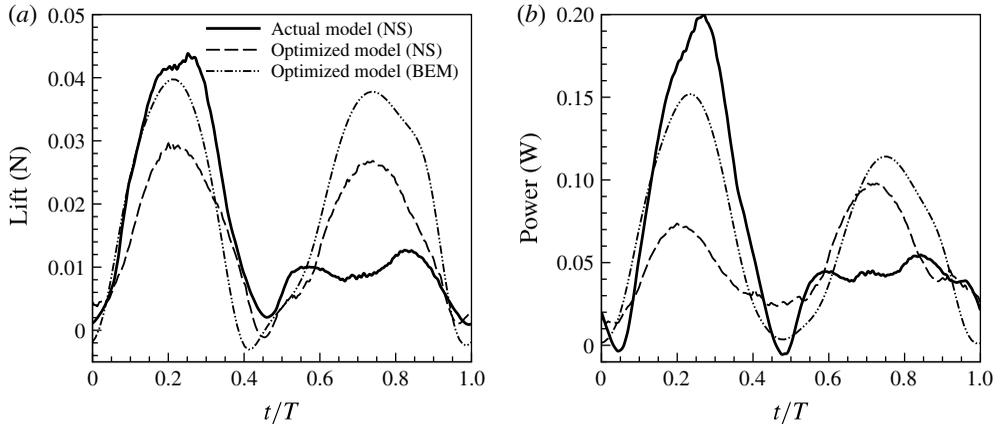
FIGURE 22. Comparison of lift (*a*) and power (*b*) during one cycle for the actual moth model as well as the optimized model identified in exercise II.

flight activity, evolved a hovering stroke that does not maximize aerodynamic efficiency? As pointed out earlier, there is no guarantee that the flight system of the hawkmoth (or any biological flyer for that matter) is designed to maximize the aerodynamic efficiency of any particular flight mode, or even of flight in general. One can however speculate as to the possible reasons for sub-optimal hovering efficiency in the hawkmoth. We note that the key difference between the hovering stroke of the moth and the optimized stroke is that while the latter has a nearly horizontal stroke plane, the former has a stroke plane with a significant angle to the horizontal. A consequence of this is that the upstroke produces relatively little (26 % of the total) lift, despite consuming 33 % of the total stoke energy. On the other hand, the more horizontal stroke for the optimized case produces nearly equal lift during both half-strokes and the energy expenditure is also more similar. There seem to be a number of possible reasons as to why the hawkmoth adopts a tilted stroke plane during hover. First, the stroke plane of the hawkmoth (as of many other flying animals) is nearly vertical during forward flight and the tilted stroke plane during hover therefore might be an evolutionary compromise between forward and hovering flight that avoids complexity in the wing joints and actuation mechanism. An alternate or additional factor may be that a tilted stroke plane during hover provides a higher level of control authority for tasks such as stabilization in unsteady environments, attitude adjustment and other maneuvers. Finally, a tilted stroke plane enables rapid transitions between forward flight and hover. Thus, it seems likely that in the hawkmoth, the aerodynamic efficiency of hover is compromised in order to simplify wing actuation and/or enhance stability and maneuverability.

5. Conclusions

A new multi-fidelity approach that couples blade-element and NS simulations has been developed. The approach is used to explore the performance of flapping insect wing strokes in a large parameter space and discover stroke patterns that are high-performing, particularly in terms of power loading. While the starting point for the current study is a stroke pattern based on a hovering hawkmoth, the method employed and tested here could be used for stroke optimization of a wide variety of biological, bioinspired or engineered flapping foil configurations.

The parameter survey of wing strokes is preceded by a comprehensive validation study that provides a clear assessment of the ability of the NS solver to predict the time-varying aerodynamic forces generated by the wing. The simulations are found to predict not only the time-mean forces, but also a variety of other measures of the time variation of the forces. This validation is based on experimental measurements of the dynamics of a freely hovering hawkmoth and demonstrates that high-speed videogrammetry coupled with carefully constructed dynamical models of the animal, enables a degree of validation that has not been attained in past studies. We expect that such validation protocols will become the standard in animal locomotion modelling studies.

We find that while the accuracy of the blade-element modelling in predicting flight forces and power cannot match that of the computationally expensive NS approach, BEM is nevertheless a useful tool for guiding NS-based optimization. In particular, the BEM predicts trends in power-loading fairly accurately, and more so than other quantities such as lift and power, and this makes BEMs particularly useful for exploring power-efficient flight strokes. A detailed comparison of the differences between the NS and BEM predictions also provides insights into the reasons that underpin the variations in predictive capability observed for the BEM. In particular, the study shows that changes in the relative timing between translation and rotation of the wing generate flow phenomena such as LEV shedding and vortex-capture which are not incorporated into the current BEM. More extensive 'tuning' of the BEM force coefficients and perhaps new models that allow for additional flow features might further improve the effectiveness of the multi-fidelity approach. However, the quasi-steady nature of the BEM makes a general solution to the discrepancies related to wing–wake interaction difficult to achieve.

Finally, we show that the flapping kinematics used by the hawkmoth is not optimal in terms of power loading, even when using a flat wing that has neither twist nor camber, and with a flapping amplitude and frequency that is constrained to that used by the animal. The flapping stroke identified as optimal by BEM resembles the condition of normal hover, and NS modelling shows that this stroke has a 33 % higher power loading than the biological stroke of the moth. The reason for the non-optimality of the biological stroke is not revealed by the current study, but is likely related to the multi-factorial nature of the optimization carried out by evolution on biological systems. For example, the tilted stroke plane used by hovering moths may be a compromise between hovering and forward flight and evolved as a way to reduce the complexity of the wing hinge. Alternatively (or in addition), the biological kinematics may provide benefits for stability or maneuverability that are not evaluated in this study. On the whole, the current study indicates that the multi-fidelity approach of combining blade-element and CFD simulations can be a useful tool for engineers to learn from Nature and guide MAV designs that may outperform natural flyers.

As noted above, all of the models in the optimization study employ rigid flat-plate wings. Past studies (Young *et al.* 2009; Nakata & Liu 2012; Dai, Luo & Doyle 2012) indicate that the flapping motion can cause significant wing deformation, which can enhance force production as well as aerodynamic efficiency. The optimization study presented in the current paper does not include these wing deformation effects. It is, however, reasonable to hypothesize that once wing flexibility is considered in wing-stroke optimization, further improvements in aerodynamic performance could be achieved. The inclusion of these effects, however, significantly expands the parameter space and creates additional challenges for computational modelling and simulation.

Acknowledgements

REFERENCES

AONO, H., SHYY, W. & LIU, H. 2009 Near wake vortex dynamics of a hovering hawkmoth. *Acta Mechanica Sin.* **25**, 23–36.

BENINI, E. & TOFFOLO, A. 2002 Optimal design of horizontal-axis wind turbines using blade-element theory and evolutionary computation. *J. Solar Energy Engng* **124**, 357–363.

BERG, H. C. 2003 The rotary motor of bacterial flagella. *Annu. Rev. Biochem.* **72**, 19–54.

BERMAN, G. J. & WANG, Z. J. 2007 Energy-minimizing kinematics in hovering insect flight. *J. Expl Biol.* **582**, 153–168.

BLAKE, R. W. 1979 The mechanics of labriform locomotion I. Labriform locomotion in the angelfish (*Pterophyllum eimekei*): an analysis of the power stroke. *J. Expl Biol.* **82**, 255–271.

BOMPHREY, R. J., LAWSON, N. J., HARDING, N. J., TAYLOR, G. K. & THOMAS, A. L. R. 2005 The aerodynamics of manduca sexta: digital particle image velocimetry analysis of the leading-edge vortex. *J. Expl Biol.* **208**, 1079–1094.

BOZKURTTAS, M., MITTAL, R., DONG, H., LAUDER, G. V. & MADDEN, P. 2009 Low-dimensional models and performance scaling of a highly deformable fish pectoral fin. *J. Fluid Mech.* **631**, 311–342.

CASEY, T. M. 1976 Flight energetics of sphinx moths: power input during hovering flight. *J. Expl Biol.* **64**, 529–543.

COMBES, S. A. & DANIEL, T. L. 2003 Into thin air: contributions of aerodynamic and inertial-elastic forces to wing bending in the hawkmoth *Manduca sexta*. *J. Expl Biol.* **206**, 2999–3006.

DAI, H., LUO, H. & DOYLE, J. F. 2012 Dynamic pitching of an elastic rectangular wing in hovering motion. *J. Fluid Mech.* **693**, 473–499.

DELAURIER, J. D. 1993 An aerodynamic model for flapping-wing flight. *Aeronaut. J.* **93**, 125–130.

DICKINSON, M. H., LEHMANN, F.-O. & SANE, S. P. 1999 Wing rotation and the aerodynamic basis of insect flight. *Science* **284**, 1954–1960.

DU, G. & SUN, M. 2010 Effects of wing deformation on aerodynamic forces in hovering hoverflies. *J. Expl Biol.* **213**, 2273–2283.

ELLINGTON, C. P. 1984 The aerodynamics of hovering insect flight. III. Kinematics. *Phil. Trans. R. Soc. Lond.* B **305**, 41–78.

ELLINGTON, C. P., VAN DEN BERG, C., WILLMOTT, A. P. & THOMAS, A. L. R. 1996 Leading-edge vortices in insect flight. *Nature* **384**, 626–630.

FLOREANO, D., ZUFFEREY, J.-C., SRINIVASAN, M. V. & ELLINGTON, C. P. 2009 *The Flying Insects and Robots*. Springer.

FRY, S. N., SAYAMAN, R. & DICKINSON, M. H. 2003 The aerodynamics of free-flight maneuvers in Drosophila. *Science* **300**, 495–498.

HEDRICK, T. L. 2008 Software techniques for two- and three-dimensional kinematic measurements of biological and biomimetic systerms. *Bioinspiration Biomimetics* **3**, 034001.

HEDRICK, T. L. & DANIEL, T. L. 2006 Flight control in the hawkmoth manduca sexta: the inverse problem of hovering. *J. Expl Biol.* **209**, 3114–3130.

VAN KAN, J. 1986 A second-order accurate pressure-correction scheme for viscous incompressible flow. *SIAM J. Sci. Stat. Comput.* **7**, 870–891.

KRISHNAKUMAR, K. 1989 Microgenetic algorithms for stationary and nonstationary function optimization. *SPIE Intelligent Control and Adaptive Systems* **1196**, 289–296.

LEHMANN, F.-O. & DICKINSON, M. H. 1997 The changes in power requirements and muscle efficiency during elevated force production in the fruit fly *Drosophila melanogaster*. *J. Expl Biol.* **200**, 1133–1143.

LIU, H. & AONO, H. 2009 Size effects on insect hovering aerodynamics: an integrated computational study. *Bioinspiration Biomimetics* **4**, 015002.

LIU, H., ELLINGTON, C. P., KAWACHI, K. & VAN DEN BERG, C. 1998 A computational fluid dynamic study of hawkmoth hovering. *J. Expl Biol.* **201**, 461–477.

MITTAL, R., DONG, H., BOZKURTTAS, M., NAJJAR, F. M., VARGAS, A. & VON LOEBBECKE, A. 2008 A versatile sharp interface immersed boundary method for incompressible flows with complex boundaries. *J. Comput. Phys.* **227**, 4825–4852.

MITTAL, R. & IACCARINO, G. 2005 Immersed boundary methods. *Annu. Rev. Fluid Mech.* **37**, 239–261.

NAKATA, T. & LIU, H. 2012 Aerodynamic performance of a hovering hawkmoth with flexible wings: a computational approach. *Proc. R. Soc.* B **279** (1729), 722–731.

NELDER, J. A. & MEAD, R. 1965 A simplex method for function minimization. *Comput. J.* **7**, 308–313.

OSBORNE, M. F. M. 1951 Aerodynamics of flapping flight with application to insects. *J. Expl Biol.* **28**, 221–245.

PENNYCUICK, C. J., HEDENSTROM, A. & ROSÉN, M. 2000 Horizontal flight of a swallow (*Hirundo rustica*) observed in a wind tunnel, with a new method for directly measuring mechanical power. *J. Expl Biol.* **203**, 1755–1765.

SANE, S. P. 2003 The aerodynamics of insect flight. *J. Expl Biol.* **206**, 4191–4208.

SANE, S. P. & DICKINSON, M. H. 2002 The aerodynamic effects of wing rotation and a revised quasi-steady model of flapping flight. *J. Expl Biol.* **205**, 1087–1096.

SEO, J. H. & MITTAL, R. 2011 A sharp-interface immersed boundary method with improved mass conservation and reduced spurious pressure oscillations. *J. Comput. Phys.* **230**, 7347–7363.

STEVENSON, R. D. & JOSEPHSON, R. K. 1990 Effects of operating frequency and temperature on mechanical power output from moth flight muscle. *J. Expl Biol.* **149**, 61–78.

SUNADA, S., SONG, D., MENG, X., WANG, H. L. & KAWACHI, K. 2002 Optical measurement of the deformation, motion, and generated forces of the wings of a moth. *JSME Int. J.* **45**, 836–842.

TANGORRA, J. L., LAUDER, G. V., HUNTER, I. W., MITTAL, R., MADDEN, P. G. A. & BOZKURTTAS, M. 2010 The effect of fin ray flexural rigidity on the propulsive forces generated by a biorobotic fish pectoral fin. *J. Expl Biol.* **213**, 4043–4054.

TRIANTAFYLLOU, G. S., TRIANTAFYLLOU, M. S. & GROSENBAUGH, M. A. 1993 Optimal thrust development in oscillating foils with application to fish propulsion. *J. Fluids Struct.* **7**, 205–224.

TU, M. S. & DANIEL, T. L. 2004 Submaximal power output from the dorsolongitudinal flight muscles of the hawkmoth manduca sexta. *J. Expl Biol.* **407**, 4651–4662.

UDAYKUMAR, H. S., MITTAL, R., RAMPUNGGOON, P. & KHANNA, 2001 A sharp interface Cartesian grid method for simulating flows with complex moving boundaries. *J. Comput. Phys.* **174**, 345–380.

USHERWOOD, J. R. & ELLINGTON, C. P. 2002 The aerodynamics of revolving wings: I. Model hawkmoth wings. *J. Expl Biol.* **205**, 1547–1564.

WALKER, J. A., THOMAS, A. L. R. & TAYLOR, G. K. 2008 Deformable wing kinematics in the desert locust: how and why do camber, twist and topography vary through the stroke?. *J. R. Sci. Interface* **6**, 735–746.

WALKER, J. A. & WESTNEAT, M. W. 2000 Mechanical performance of aquatic rowing and flying. *Proc. R. Soc. Lond.* B: *Biol. Sci.* **267**, 1875–1881.

WANG, H., ANDO, N. & KANZAKI, R. 2008 Active control of free flight manoeuvres in a hawkmoth, *Agrius convolvuli*. *J. Expl Biol.* **211**, 423–432.

WANG, H., ZENG, L., LIU, H. & YIN, C. 2003 Measuring wing kinematics, flight tranjectory and body attitude during forward flight and turing maneauvers in dragonflies. *J. Expl Biol.* **206**, 745–757.

WARRICK, D. R., TOBALSKE, B. W. & POWERS, D. R. 2005 Aerodynamics of the hovering hummingbird. *Nature* **23**, 1094–1097.

WEIS-FOGH, T. 1973 Estimates of flight fitness in hovering animals, including novel mechanisms for lift production. *J. Expl Biol.* **59**, 169–230.

WILLMOTT, A. P. & ELLINGTON, C. P. 1997a The mechanics of flight in the hawkmoth manduca sexta: I. Kinematics of hovering and forward flight. *J. Expl Biol.* **200**, 2705–2722.

WILLMOTT, A. P. & ELLINGTON, C. P. 1997b The mechanics of flight in the hawkmoth manduca sexta: II. Aerodynamic consequences of kinematic and morphological variation. *J. Expl Biol.* **200**, 2723–2745.

WILLMOTT, A. P., ELLINGTON, C. P. & THOMAS, A. L. R. 1997 Flow visualization and unsteady aerodynamics in the flight of the hawkmoth, manduca sexta. *Phil. Trans. R. Soc. Lond.* B **352**, 303–316.

WOOD, R. 2008 The first takeoff of a biologically inspired at-scale robotic insect. *IEEE Trans. Robot.* **24**, 341–347.

YE, T., MITTAL, R., UDAYKUMAR, H. S. & SHYY, W. 1999 An accurate Cartesian grid method for viscous incompressible flows with complex immersed boundaries. *J. Comput. Phys.* **156**, 209–240.

YOUNG, J., WALKER, S. M., BOMPHREY, R. J., TAYLOR, G. K. & THOMAS, A. L. R. 2009 Details of insect wing design and deformation enhance aerodynamic function and flight efficiency. *Science* **325**, 1549–1552.

ZANG, Y., STREET, R. L. & KOSEFF, J. R. 1994 A non-staggered grid, fractional step method for time-dependent incompressible Navier–Stokes equations in curvilinear coordinates. *J. Comput. Phys.* **114**, 18–33.

ZENG, L., HAO, Q. & KAWACHI, K. 2000 A scanning projected line method for measuring a beating bumblebee wing. *Opt. Commun.* **183**, 19–44.

ZHENG, L., MITTAL, R. & HEDRICK, T. L. 2013 Time-varying wing-twist improves aerodynamic efficiency of forward flight in butterflies. *PLoS ONE* **8** (1), e53060.